Article

Structure

A Structural Model for Vinculin Insertion into PIP_2-Containing Membranes and the Effect of Insertion on Vinculin Activation and Localization

Graphical Abstract

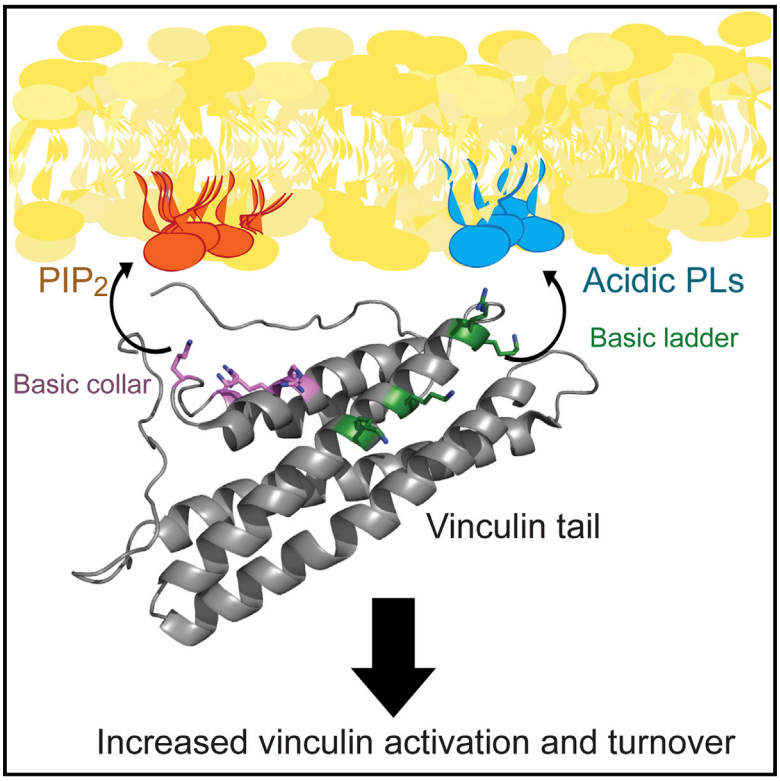

Authors

Peter M. Thompson,
Srinivas Ramachandran,
Lindsay B. Case, ...,
Nikolay V. Dokholyan,
Clare M. Waterman,
Sharon L. Campbell

Correspondence

campbesl@med.unc.edu

In Brief

Vinculin is a cytoskeletal protein that controls cellular adhesion and migration. Thompson et al. show that two basic patches on the tail domain cooperate to bind lipid membranes containing PIP_2. These binding events regulate vinculin activation and turnover at focal adhesions.

Highlights

- The vinculin tail contains two basic patches with distinct lipid binding roles
- The basic collar recognizes PIP_2
- The basic ladder recognizes acidic phospholipids
- Lipid binding increases vinculin activation and turnover at focal adhesions

Thompson et al., 2017, Structure *25*, 1–12
February 7, 2017
http://dx.doi.org/10.1016/j.str.2016.12.002

CellPress

Please cite this article in press as: Thompson et al., A Structural Model for Vinculin Insertion into PIP_2-Containing Membranes and the Effect of Insertion on Vinculin Activation and Localization, Structure (2016), http://dx.doi.org/10.1016/j.str.2016.12.002

A Structural Model for Vinculin Insertion into PIP_2-Containing Membranes and the Effect of Insertion on Vinculin Activation and Localization

Peter M. Thompson,[1,6] Srinivas Ramachandran,[1,7] Lindsay B. Case,[2,8] Caitlin E. Tolbert,[3,9] Arpit Tandon,[1] Mihir Pershad,[4] Nikolay V. Dokholyan,[1,5] Clare M. Waterman,[2,8] and Sharon L. Campbell[1,5,10,*]

[1]Department of Biochemistry and Biophysics, University of North Carolina at Chapel Hill, Chapel Hill, NC 27599, USA
[2]Cell Biology and Physiology Center, National Heart Lung and Blood Institute, National Institutes of Health, Bethesda, MD 20892, USA
[3]Department of Cell Biology and Physiology
[4]Department of Chemistry
[5]Lineberger Comprehensive Cancer Center
University of North Carolina at Chapel Hill, Chapel Hill, NC 27599, USA
[6]Present address: Laboratory of Genome Integrity and Structural Biology, National Institute of Environmental Health Sciences, Research Triangle Park, NC 27709, USA
[7]Present address: Division of Basic Sciences, Fred Hutchinson Cancer Research Center, Seattle, WA 98109, USA, USA
[8]Present address: Department of Biophysics, University of Texas Southwestern Medical Center, Dallas, TX 75390, USA
[9]Present address: Cellular Signaling and Cytoskeletal Function Lab, Francis Crick Institute, London NW1 1AT, UK
[10]Lead Contact
*Correspondence: campbesl@med.unc.edu
http://dx.doi.org/10.1016/j.str.2016.12.002

SUMMARY

Vinculin, a scaffolding protein that localizes to focal adhesions (FAs) and adherens junctions, links the actin cytoskeleton to the adhesive super-structure. While vinculin binds to a number of cytoskeletal proteins, it can also associate with phosphatidylinositol 4,5-bisphosphate (PIP_2) to drive membrane association. To generate a structural model for PIP_2-dependent interaction of vinculin with the lipid bilayer, we conducted lipid-association, nuclear magnetic resonance, and computational modeling experiments. We find that two basic patches on the vinculin tail drive membrane association: the basic collar specifically recognizes PIP_2, while the basic ladder drives association with the lipid bilayer. Vinculin mutants with defects in PIP_2-dependent liposome association were then expressed in vinculin knockout murine embryonic fibroblasts. Results from these analyses indicate that PIP_2 binding is not required for localization of vinculin to FAs or FA strengthening, but is required for vinculin activation and turnover at FAs to promote its association with the force transduction FA nanodomain.

INTRODUCTION

Vinculin (Vcl) is a large (117 kDa), ubiquitously expressed and highly conserved scaffolding protein present in higher eukaryotes. It localizes to focal adhesions (FAs) and adherens junctions (Johnson et al., 1998), and has been implicated in regulating cell morphology, cell migration (Coll et al., 1995), cell stiffness (le Duc et al., 2010; Shen et al., 2011), adhesion strength (Mierke et al., 2008), FA turnover, and FA morphology (Xu et al., 1998a, 1998b).

Vcl contains an N-terminal head domain (Vh) and a C-terminal tail domain (Vt) connected by a proline-rich linker (Bakolitsa et al., 2004). Vh and Vt bind each other and maintain Vcl in an autoinhibited conformation (Bakolitsa et al., 2004; Cohen et al., 2005; Johnson and Craig, 1995b). Release of autoinhibition occurs via binding of ligands and possibly phosphorylation (Chen et al., 2006; Golji et al., 2012). While Vcl has been shown to associate with ~20 binding partners, the tail domain alone binds filamentous actin (F-actin) (Huttelmaier et al., 1997) and acidic phospholipids (Johnson and Craig, 1995a), specifically phosphatidylinositol 4,5-bisphosphate (PIP_2) (Palmer et al., 2009). These tail domain interactions are believed to coordinate with Vh interactions to facilitate Vcl activation (Weekes et al., 1996).

In FAs, PIP_2 is generated by phosphatidylinositol phosphate kinase type 1 gamma (PIPKIγ) (van den Bout and Divecha, 2009) and, through PIP_2 production, PIPKIγ regulates FA dynamics (Li et al., 2013; Wu et al., 2011). PIP_2 is also required for FA formation (Sun et al., 2007) and promotes recruitment and activation of Vcl at FAs (Legate et al., 2011; Wu et al., 2011). However, the consequences of the Vcl/PIP_2 interaction are less clear. While association of Vcl with PIP_2 has been implicated in numerous processes including cell spreading, cell migration, FA turnover, and force transduction (Chandrasekar et al., 2005; Chinthalapudi et al., 2014; Diez et al., 2009; Saunders et al., 2006), the Vcl constructs used in these studies may not be selective in their disruption of PIP_2 binding. In addition, PIP_2 has been reported to regulate Vcl phosphorylation (Ziegler et al., 2002) and trafficking (Halstead et al., 2010; Marquez et al., 2009).

Vt contains two strongly basic surfaces, the basic ladder and the basic collar (Figure 1) (Bakolitsa et al., 1999). Mutation of the basic collar (Bakolitsa et al., 2004; Chinthalapudi et al., 2014;

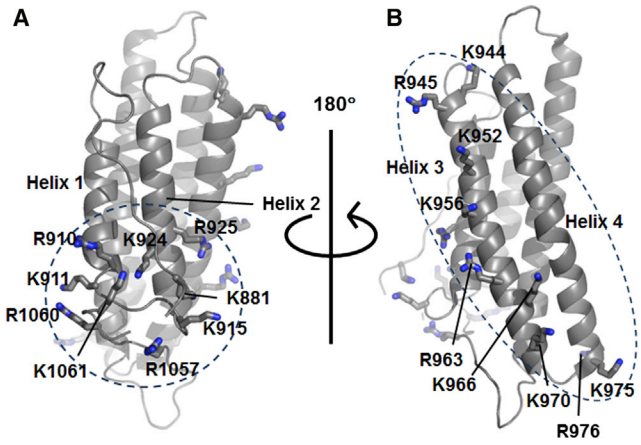

Figure 1. Vt Contains Two Basic Regions Predicted to Bind PIP_2

(A) Ribbon diagram of Vt (PDB: 1ST6) highlighting basic collar residues within the N-terminal strap, helices 1 and 2, and the C terminus.

(B) Ribbon diagram of Vt (PDB: 1ST6) highlighting basic ladder residues within helices 3 and 4.

Saunders et al., 2006; Ziegler et al., 2002), the basic ladder (Chandrasekar et al., 2005; Chinthalapudi et al., 2014), or deletion of the C terminus (Chandrasekar et al., 2005; Diez et al., 2009; Saunders et al., 2006; Wirth et al., 2010; Ziegler et al., 2002) impairs PIP_2 binding. However, the use of multiple mutations or deletions within Vt can alter its structure and perturb other Vt functions (Palmer et al., 2009). For example, two separate Vcl variants with reported PIP_2 defects of comparable severity, Vcl K952Q/K956Q/R963Q/R966Q and Vcl R1060Q/K1061Q, exhibit different phenotypes in exerting force on a substrate (Diez et al., 2009).

Recently, a crystal structure of a Vt mutant bound to a soluble, short-chain PIP_2 was solved, providing the first structural model for how PIP_2 binds to Vt (PDB: 4PR9) (Chinthalapudi et al., 2014). In the structure, Vt R1060A forms a trimeric oligomer when bound to 1,2-dioctanoyl-*sn*-glycero-3-phospho-(1′-myo-inositol-4′,5′-bisphosphate) (PIP_2-C8). Two of the Vt molecules recognize the PIP_2 head group via the basic collar, whereas the third Vt molecule interacts with the PIP_2 head group through residues K944 and R945 in the basic ladder. Mutations to the basic collar (Vt K1061Q) or the basic ladder (K944Q/R945Q) disrupt PIP_2-dependent lipid co-sedimentation (Chinthalapudi et al., 2014). Later work confirmed that Vt dimerizes in the presence of PIP_2 (Chinthalapudi et al., 2015). However, these models fail to explain how PIP_2 association with Vt promotes membrane insertion. In addition, the two lipid-disrupting mutants produced distinct phenotypes when expressed in Vcl-null mouse embryonic fibroblasts ($Vcl^{-/-}$ MEFs). Whereas Vcl K944Q/R945Q prevents exchange of Vcl at FAs, Vcl K1061Q only mildly disrupts exchange of Vcl at FAs (Chinthalapudi et al., 2014).

Using computational modeling, site-directed mutagenesis, and lipid co-sedimentation of Vt in membrane mimetics, we confirm that both the basic ladder and collar are involved in binding to acidic phospholipids. However, our data suggest an alternative structural model: the basic collar promotes PIP_2-specific binding while the basic ladder drives membrane insertion. Cells expressing Vcl variants specifically deficient in lipid binding retain the ability to reinforce cell stiffness upon mechanical deformation, but show altered FA turnover, perturbed nanoscale Vcl localization within FAs, and reduced Vcl activation at FAs.

RESULTS

Computational Modeling Predicts Distinct Roles for the Basic Collar and Basic Ladder

To better understand how Vt binds PIP_2, we modeled the interaction of the PIP_2 head group with Vt. The head group, D-inositol 4,5-bisphosphate, was docked to Vt residues 895–1,065 using MedusaDock (Ding et al., 2010; Yin et al., 2008). The N-terminal strap was omitted from Vt for docking, as its removal retains the Vt fold and actin binding, but increases association with PIP_2 (Palmer et al., 2009). MedusaDock identified the basic collar, specifically residues R910, K915, K924, and R925, as the Vt site with the highest specificity for the PIP_2 head group. The side chain of R910 interacts primarily with the hydroxyl of C4, K915 with the hydroxyl of C6 (which would place it near the phosphoryl group on C1 in the full PIP_2 molecule), K924 with the hydroxyl of C5, and R925 with the phosphoryl group on C4 (Figure 2A).

Next, discrete molecular dynamics (DMD) simulations (Ding et al., 2008; Dokholyan et al., 1998; Shirvanyants et al., 2012) were performed with a full-length PIP_2, 1-stearoyl-2-arachidonoyl-*sn*-glycero-3-phospho-(1′-myo-inositol-4′,5′-bisphosphate), constraining the PIP_2 head group to the basic collar and using Gō constraints on Cβ/Cα contacts (with the interaction square-well depth 0.5ε, where ε is the DMD energy unit [Dokholyan et al., 1998; Proctor et al., 2011]) for all residues in Vt (residues 896–1,065) or Gō constraints only for residues in α helices (using Vt constructs 896–1,065 or 896–1,059). After selecting 2,000 snapshots with a binding energy less than −10 kcal/mol (Ding et al., 2010), the residues in contact with PIP_2 were tallied (Figure 2B). In all cases, the contacts at the basic collar remained high. When using Gō constraints only for helical residues, some contacts were observed at the basic ladder, although contacts at the basic collar were more frequent (Figure 2B). For more complete sampling of full-length PIP_2 binding Vt, we performed DMD simulations in which the PIP_2 head group was unrestrained. In these simulations, we see PIP_2 sampling all regions of Vt, which argues against the head group binding the basic collar being a kinetically trapped state. We clustered the DMD snapshots. Four of the seven clusters feature the head group interacting with the basic collar (Figure S1A). Furthermore, the largest cluster of conformations recapitulates head group interactions with the basic collar that were seen in the docking simulations (Figure S1B).

While both MedusaDock and DMD simulations identify the basic collar as the primary site for PIP_2 head group recognition, these simulations were performed in the absence of a lipid bilayer. To better mimic the physiological interaction at the membrane, all-atom, explicit solvent molecular dynamics simulations of Vt bound to PIP_2 in a 1-palmitoyl-2-oleoyl-*sn*-glycero-3-phosphocholine (POPC) bilayer were conducted. At the start of the simulation, Vt (residues 896–1,055) was bound to PIP_2 as in the docking pose (Figure 2A) and the Vt helix bundle was

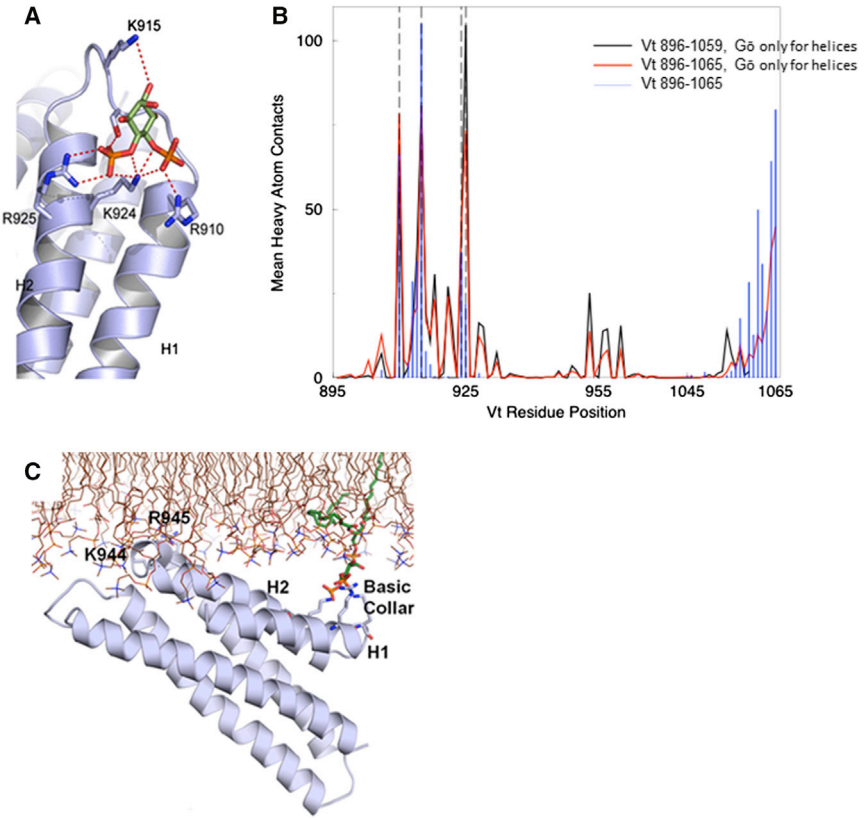

Figure 2. Simulations of PIP_2-Mediated Vt Membrane Association Identify Distinct Roles for the Basic Collar and Basic Ladder

(A) MedusaDock results displaying PIP_2 head group (green) interactions with the Vt basic collar.

(B) Results from DMD simulations of 1-stearoyl-2-arachidonoyl-*sn*-glycero-3-phospho-(1′-myo-inositol-4′,5′-bisphosphate) with Vt. The average number of heavy atom Vt contacts with PIP_2 are mapped per residue for simulations with Gō constraints for helices and Vt 896–1,059 (black), Vt 896–1,065 (red), and Gō constraints for all Vt residues 896–1,065 (blue). R910, K915, K924, and R925 are denoted with dashed vertical lines.

(C) GROMACS simulation results (final pose) of Vt, in the presence of POPC and one molecule of PIP_2 (green carbons). The basic collar, helices 1 and 2, and K944 and R945 are labeled. See also Figures S1 and S2 and Movies S1, S2, and S3.

oriented roughly parallel to the lipid bilayer. We performed three simulations of 100 ns each. In all three simulations, the contacts between basic collar and PIP_2 head group were maintained, even as the PIP_2 molecule diffused around in the bilayer (Figure S2A). Furthermore, helix 3 of Vt was found to contact the bilayer in all three simulations. The side chains of basic ladder residues K944, R945, K952, and K956 inserted into the lipid bilayer (Figure 2C, Movies S1 and S2). We also performed three 100 ns simulations of Vt in the same starting configuration in a POPC-only bilayer. In these control simulations, basic collar interactions with the membrane were not observed and interactions of helix 3 with the membrane were inconsistent. In one of the three simulations, Vt diffuses away from the membrane (Movie S3). The control simulations confirm that PIP_2 anchors Vt to the membrane through the basic collar, which facilitates basic ladder interactions with the bilayer.

Short-Chain PIP_2 Binds to Vt at a Hydrophobic Patch on Helices 4 and 5 in Solution

The mode of binding of Vt to membrane-associated PIP_2 from our simulations (Figure 2C) is significantly different from the recently published crystal structure of Vt R1060A complexed to a short-chain PIP_2 lipid (PIP_2-C8) (Chinthalapudi et al., 2014) and the model docked to a lipid bilayer (Chinthalapudi et al., 2015). Chinthalapudi et al. (2014, 2015) show that the sidechain of K1061 binds to the PIP_2 head group, but not R910 and R925, which interact in our model. In addition, the proposed orientations of membrane-associated Vt molecules within a dimer do not match our modeled orientation. A possible explanation for this discrepancy is the use of PIP_2-C8 instead of PIP_2 contained in a lipid bilayer. We titrated ^{15}N-enriched Vt with PIP_2-C8 at various ratios and monitored nuclear magnetic resonance (NMR) spectral changes by 2D ^{1}H-^{15}N heteronuclear single-quantum coherence (HSQC) analyses (Figure 3A). In doing so, we hoped to avoid potential artifacts from crystallization and use of the R1060A mutant. At Vt:PIP_2-C8 ratios of 1:2.5 and 1:6 a white precipitate formed, as previously reported (Chinthalapudi et al., 2015), suggesting that Vt was saturated with PIP_2-C8 at a ratio of 1:2.5. Perturbations in chemical shift or line width map to a site on helices 3, 4, and 5, were comprised primarily by a hydrophobic patch. Peaks corresponding to these residues significantly shift or broaden, suggesting a strong interaction (Figures 3B–3D). In contrast, peaks corresponding to residues in the basic collar do not significantly shift or broaden with increasing PIP_2-C8 (Figures 3B–3D). Weaker shifts are found in peaks corresponding to the basic ladder. These results suggest that the fatty acid tails of PIP_2-C8 drive binding in solution, and that the PIP_2 head group associates with the basic ladder because of its proximity to the hydrophobic patch. An interaction between the acyl chains and the hydrophobic patch was not observed in the crystal structure of the Vt:PIP_2-C8 complex (Chinthalapudi et al., 2014).

PIP_2 was also deemed sufficient for the generation of Vt oligomers (Chinthalapudi et al., 2014, 2015). To test the ability PIP_2-C8 to induce Vt oligomerization in solution we used TROSY for a rotational correlation times (TRACT) NMR experiment (Lee et al., 2006) to calculate the effective rotational correlation time of Vt (Figure 4). Oligomerization of Vt would slow tumbling and significantly increase the rotational correlation time. However, the rotational correlation time of Vt did not increase at a 1:1 ratio of Vt:PIP_2-C8, suggesting that either Vt does not oligomerize in the presence of PIP_2-C8 or that Vt oligomers induced by binding PIP_2-C8 are unobservable by solution NMR. Such oligomers would either be insoluble or large multimers with very fast

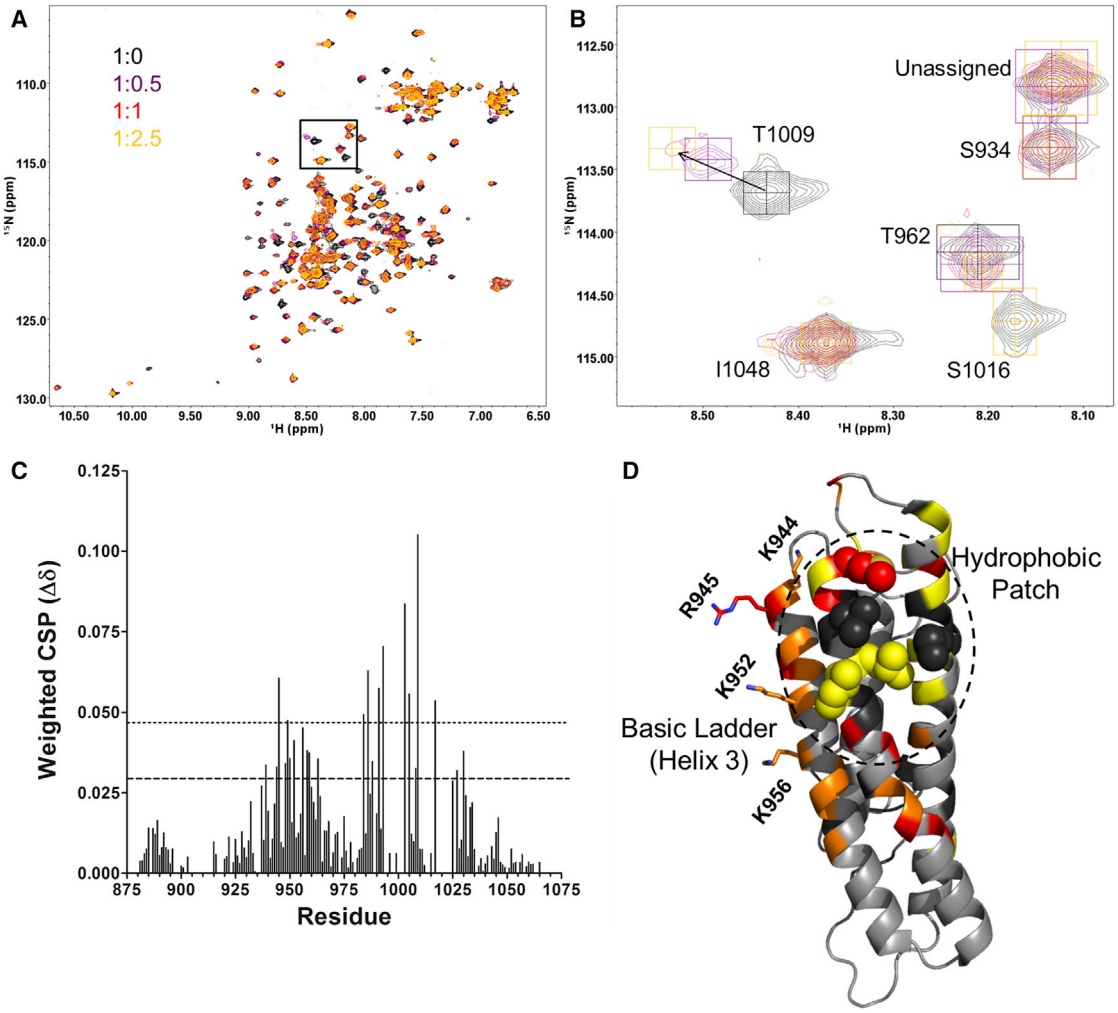

Figure 3. Titration of ^{15}N-Enriched Vt with PIP_2-C8

(A and B) 2D NMR ^{1}H-^{15}N HSQC titration of PIP_2-C8 into ^{15}N-enriched Vt (50 μM) at the listed ratios. The inset (B) shows an expanded view of the T1009, S1016, and I1048 resonances. The T1009 amide peak undergoes chemical shift changes (see arrow) and the S1016 peak shows line width broadening; the I10148 resonance is unperturbed.

(C) The weighted chemical shift perturbation (CSP) is shown for each assigned residue. The dashed line corresponds to the average CSP plus 1 SD, while the dotted line corresponds to the average CSP plus 2 SDs.

(D) CSP and line broadening changes mapped to the Vt structure. Residues with CSP greater than twice the SD from the mean are shown in red. Those with CSP greater than 1 SD from the mean but less than two are shown in orange. Residues in yellow broaden significantly and are difficult to track. Residues in black are unassigned. K944, R945, K952, and K956, which reside in the basic ladder are shown as sticks. Aliphatic residues in the hydrophobic patch on helices 4 and 5 are shown as spheres.

magnetic relaxation. These explanations are inconsistent with a functional Vt dimer or trimer, suggesting that PIP_2-C8 is insufficient to appropriately study the Vt:PIP_2 interaction.

The R1060Q/K1061Q PIP_2-Deficient Vt Variant Is a Poor Actin Crosslinker

The Vcl variant, LD-CT (Vcl R1060Q/K1061Q), has been used in multiple studies as a lipid-binding-deficient Vcl construct (Chandrasekar et al., 2005; Diez et al., 2009; Ziegler et al., 2002). High-speed co-sedimentation assays revealed that Vt LD-CT retains actin binding (Figure S3), while low-speed actin co-sedimentation assays show that Vt LD-CT is deficient in F-actin crosslinking (Figure S3).

The Basic Collar Is Required for Lipid Binding and F-Actin Crosslinking

As our molecular dynamics simulations indicate that R910, K915, K924, and R925 play key roles in binding the PIP_2 head group, we measured PIP_2 binding of Vt K924A/R925A (Vt BC_2A) and Vt R910A/K915A/K924A/R925A (Vt BC_4A) using a PIP_2 co-sedimentation assay (Palmer et al., 2009). While Vt BC_2A exhibited a modest decrease in binding to PIP_2, with roughly half as much Vt binding at 5% PIP_2 (Figure 5A), Vt BC_4A showed an even greater drop in PIP_2 binding, with a 6-fold decrease in binding at 5% PIP_2. These findings suggest that the basic collar residues R910, K915, K924, and R925 are important for PIP_2 binding.

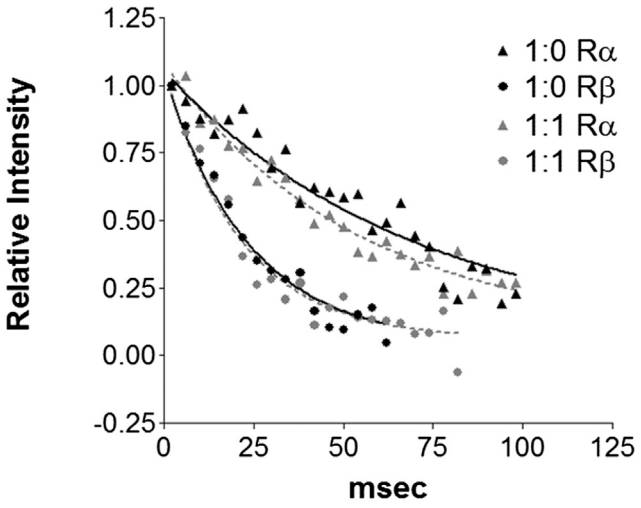

Vt:PIP_2	1:0	1:1
R_α (s^{-1})	14.34 ± 2.23	18.65 ± 2.05
R_β (s^{-1})	42.22 ± 6.76	46.36 ± 6.57
Difference	27.88 ± 8.99	27.71 ± 8.62
Correlation time (ns)	11.31 ± 3.03	11.27 ± 2.72

Figure 4. Rotational Correlation Time of Vt Is Not Altered upon Binding of PIP_2-C8

A 1D plot of amide resonance intensity determined from the TRACT experiment at two different Vt:PIP_2 ratios. The curves were analyzed for different relaxation rates and the effective rotational correlation time was calculated. At both ratios, Vt exhibited a correlation time of roughly 11.3 ns.

We found that both Vt BC_2A and Vt BC_4A retain actin binding (Figure 5B), consistent with the current structural model of the Vt/actin complex (Kim et al., 2014). However, these variants exhibited a significant decrease in the ability of Vt to bundle F-actin filaments, as measured by a low-speed co-sedimentation assay (Figure 5C). This decrease was not rescued by the more conservative Vt variant, Vt BC_4Q (R910Q/K915Q/K924Q/R925Q) (Figure 5E), suggesting that retention of the basic collar-positive charge is important for bundling of F-actin by Vcl.

The Basic Ladder Is Required for Lipid Association

Since mutations to the basic collar disrupt the ability of Vt to bundle F-actin, Vcl variants with mutations in the basic collar cannot be used to specifically report on the role of lipid binding by Vcl in cells. Mutation of basic residues within the Vt basic ladder can also disrupt binding to PIP_2-containing liposomes (Chandrasekar et al., 2005; Chinthalapudi et al., 2014), suggesting that these residues may be good targets for disrupting PIP_2 binding. Three constructs were generated to test the importance of the basic ladder in binding to PIP_2-containing liposomes: Vt K944A/R945A (BL_2A), Vt K944A/R945A/K952A (BL_3A), and Vt K944A/R945A/K952A/K956A (BL_4A). All three constructs all show decreased binding to PIP_2-containing liposomes (Figure 6A), with Vt BL_4A exhibiting the most severe defect.

Actin-binding and crosslinking activities for these variants were evaluated to test the specificity of the PIP_2 binding defect. Vt BL_2A, Vt BL_3A, and Vt BL_4A all retain actin binding (Figure 6B) and crosslinking (Figure 6C). These data support the use of these basic ladder variants in studying the biological function of the Vcl/PIP_2 interaction.

The Vt Basic Ladder Drives Association with Acidic Liposomes

As mutations in both the basic collar and basic ladder impair Vt binding to PIP_2-containing liposomes, it is difficult to determine which site is responsible for PIP_2 specificity. Co-sedimentation experiments conducted with Vt BC_4Q or Vt BL_4A and increasing amounts of PIP_2 showed similar association profiles (Figure 7A). We tested the hypothesis that the basic ladder is critical for membrane insertion by performing lipid co-sedimentation assays in the absence of PIP_2, but with increasing concentrations of phosphatidylserine (PS). Wild-type (WT) Vt bound to these liposomes in a PS-dependent manner, with nearly 70% of Vt bound when the liposomes contained 60% PS (Figure 7B). Vt BC_4Q retained some binding, with 15% of Vt BC_4Q associated with 60% PS-containing liposomes. However, Vt BL_4A did not show significant binding, even at high levels of PS, suggesting that the basic ladder drives interactions with negatively charged lipid membranes. As mutations within the N-terminal half of helix 3 impair lipid association yet retain actin interactions, these variants are reasonable tools to study the effect of lipid binding by Vcl in cells.

Lipid Binding Regulates Vcl Nanoscale Localization, Activation, and Turnover in FAs

Our structural and biochemical characterization of Vt basic collar and ladder mutants identified a Vcl variant with a specific lipid binding deficiency to facilitate studies of Vcl lipid association in a cellular context. We expressed Vcl WT, Vcl BL_2A, or Vcl BL_4A in $Vcl^{-/-}$ MEFs and plated them on fibronectin (FN)-coated coverslips. Tagging with GFP revealed that Vcl BL_2A and Vcl BL_4A still localize to FAs (Figure S4A). Because Vcl nanoscale localization within FAs has been shown to correlate with Vcl function (Case et al., 2015), we utilized iPALM, a super-resolution fluorescence microscopy technique that provides nanometer (10–20 nm) localization accuracy of individual proteins (Case et al., 2015; Kanchanawong et al., 2010) to determine the nanoscale position of tandem-Eos Vcl BL_4A in FAs. Previous studies have established protein localization to three nanodomains organized along the z axis in FAs: the membrane proximal integrin signaling layer (25–54 nm from the extracellular matrix [ECM] on the coverslip surface) where Vcl is initially recruited and activated; the force transduction layer (55–84 nm from the ECM) where active Vcl interacts with talin and strengthens FAs; and the actin regulatory layer (85–150 nm from the ECM) where Vcl binds actin (Case et al., 2015; Case and Waterman, 2015). iPALM analysis showed that while Vcl WT molecules had a median localization of 70 nm above the ECM, as reported previously (Case et al., 2015; Kanchanawong et al., 2010; Liu et al., 2015), Vcl BL_4A molecules localized significantly deeper at a median distance of 80 nm above the ECM. This change in distribution of Vcl BL_4A relative to Vcl WT was driven by a loss of molecules from the force transduction

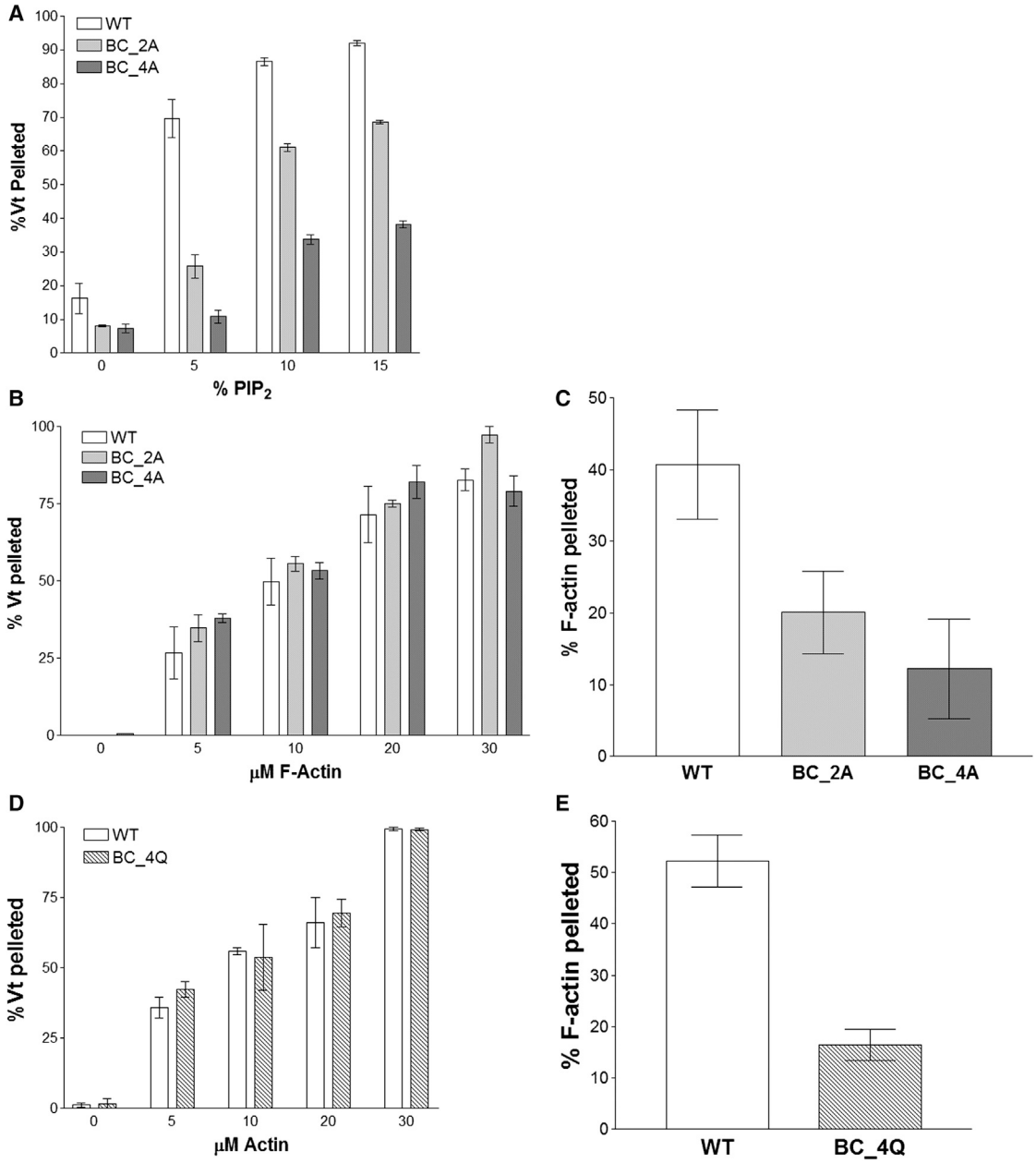

Figure 5. Mutations within the Vt Basic Collar Disrupt PIP_2 Binding and F-Actin Crosslinking

(A) Liposome co-sedimentation assay. Mutations in the Vt basic collar disrupt binding to PIP_2-containing liposomes.

(B–E) Actin co-sedimentation assays. At high-speed co-sedimentation (B) and (D) the Vt basic collar mutants retain actin binding, but at low-speed co-sedimentation (C) and (E) a decrease in F-actin crosslinking is observed. n $\geq$ 3, error bars are ±SEM. See also Figure S3.

layer and re-localization to the actin regulatory layer (Figure 8E). These results suggest that lipid binding plays a role in regulating Vcl's vertical position in the FA, promoting its association with the force transduction layer and likely F-actin.

As PIP_2 binding contributes to Vcl activation in vitro (Bakolitsa et al., 1999, 2004bib_Bakolitsa_et_al_1999; Izard et al., 2004; Weekes et al., 1996), and Vcl activation promotes a shift of Vcl from the force transduction layer to the actin regulatory layer of the FA (Case et al., 2015), we employed a Förster resonance energy transfer (FRET)-based biosensor designed to monitor the activation state of Vcl (Case et al., 2015; Chen et al., 2005) in $Vcl^{-/-}$ MEFs, to determine if disruption of PIP_2 binding alters Vcl activation. The biosensor exhibits a low FRET ratio when Vcl is active and a high FRET ratio when Vcl is inactive (Case et al., 2015; Chen et al., 2005). The FRET ratio for Vcl WT was significantly lower in FAs than the ratio in the cytoplasm, indicating that a substantial fraction of Vcl WT is activated at FAs (Case et al., 2015; Ling et al., 2002). In contrast, Vcl variants Vcl BL_2A and Vcl BL_4A exhibited higher FRET ratios in FAs, closer to values obtained in the cytoplasm. In addition, the

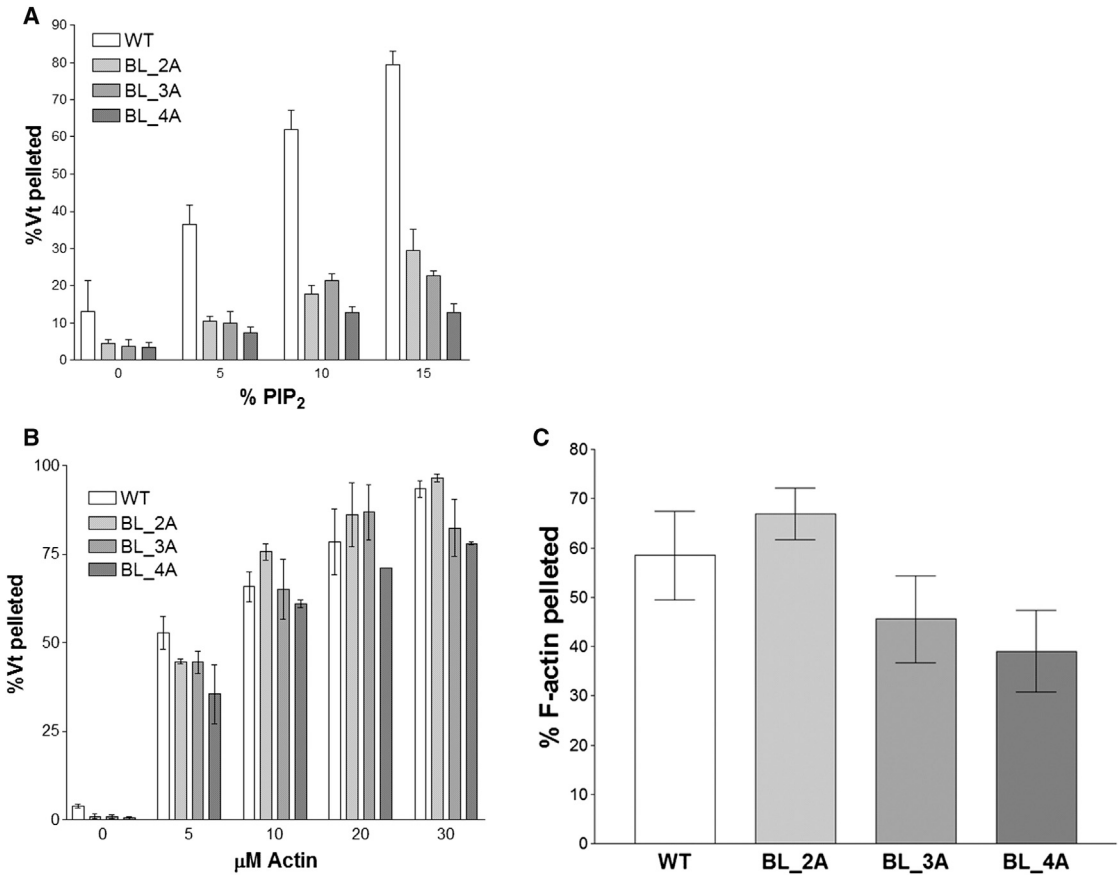

Figure 6. Mutations to the Basic Ladder Disrupt PIP_2 Binding but Do Not Significantly Impair F-Actin Binding or Crosslinking

(A) Liposome co-sedimentation assay. Mutation of the basic ladder disrupts binding to PIP_2-containing liposomes.

(B and C) Actin co-sedimentation assays. Basic ladder mutants retain F-actin binding and crosslinking (bundling), respectively, as determined by high-speed co-sedimentation (B) and low-speed co-sedimentation (C). $n \geq 3$, error bars are ±SEM.

FRET ratio in FAs for Vcl WT was significantly lower than the FRET ratio in FAs for Vcl BL_4A. These results suggest that Vcl membrane association plays an important role in activating Vcl at FAs.

Previous studies have reported conflicting results regarding whether PIP_2 binding contributes (Chinthalapudi et al., 2014; Saunders et al., 2006) or not (Chandrasekar et al., 2005) to Vcl binding to and dissociation from FAs, which is related to cell migration. We used fluorescence recovery after photobleaching (FRAP) experiments to monitor the relative amount of mobile and immobile GFP-tagged Vcl at FAs and to measure its dissociation from FAs ($T_{1/2}$ of recovery) in MEFs. Our data showed that lipid binding significantly increased the fraction of Vcl that remained stably bound and immobile within FAs (Figure 8H). Indeed, GFP-Vcl BL_4A fluorescence at FAs recovered by 75% after photobleaching in our FRAP assays, while only 60% of GFP-Vcl WT fluorescence recovered. An intermediate amount, 68%, of Vcl BL_2A recovered at FAs, although this was not significantly different from Vcl WT or Vcl BL_4A. Examination of the $T_{1/2}$ of recovery showed that, contrary to the work of Chinthalapudi et al., lipid binding did not affect the rate of Vcl dissociation from FAs (Figure 8). These results indicate that Vcl binding to PIP_2 promotes the turnover of Vcl at FAs, but not the rate of Vcl dissociation, by decreasing the immobile fraction of Vcl. This is consistent with previous work, as constitutively active Vcl is less mobile (Cohen et al., 2006).

Vcl Lipid Binding Does Not Regulate Cell Spread Area, FA Size, FA Number, or Response to External Forces at FAs

While the Vcl/PIP_2 interaction contributes to Vcl activation, localization, and turnover at FAs, it has also been reported to have a critical role in FA number, morphology, and force sensing (Chandrasekar et al., 2005; Diez et al., 2009). To test this, we expressed N-terminally GFP-tagged Vcl WT, Vcl BL_2A, and Vcl BL_4A in $Vcl^{-/-}$ MEFs and monitored the number and size of FAs as well as cell spread area (Figure S4). No significant differences were observed, suggesting that lipid binding by Vcl does not have a large impact on the general maintenance of FAs or cell spreading.

Previous work has reported that loss of lipid binding by Vcl impairs the cellular response to force (Diez et al., 2009). However, these measurements were made using Vcl LD-CT, a poor actin bundler (Figure S3B). Using 3D force microscopy, we evaluated the ability of cells expressing our Vcl constructs to respond to external forces on integrins. FN-coated magnetic beads were

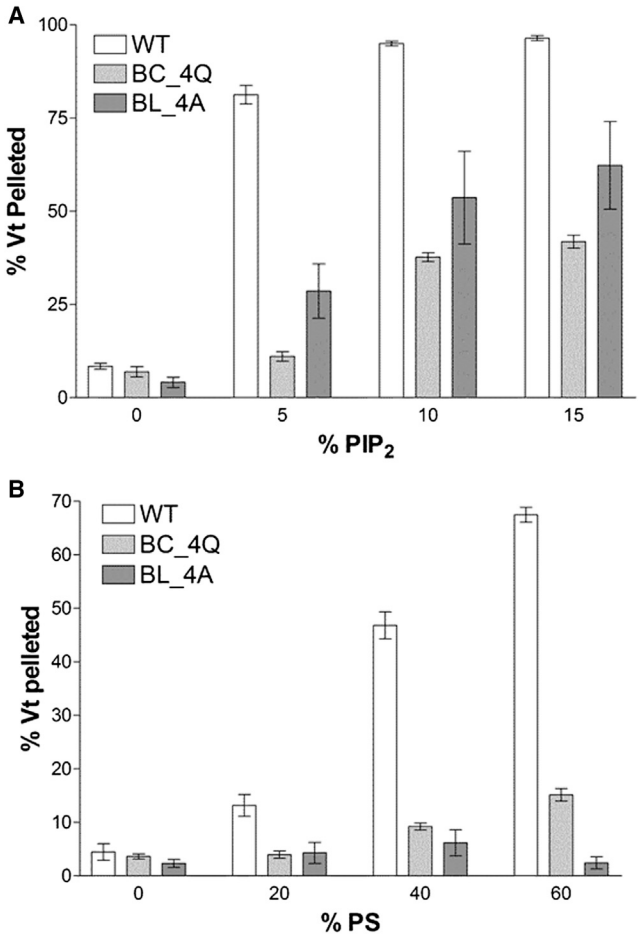

Figure 7. Comparative Lipid Co-sedimentation Assays for Vt BC_4Q and Vt BL_4A

(A) Lipid co-sedimentation assay with PIP_2-containing liposomes. Mutations within the Vt basic collar (Vt BC-4Q) or basic ladder (Vt BL-4A) disrupt binding to PIP_2-containing liposomes

(B) Lipid co-sedimentation assay with PS-containing liposomes. Mutations within the Vt basic collar (Vt BC-4Q) or basic ladder (Vt BL-4A) disrupt binding to PS-containing liposomes. Larger defects in PS-dependent lipid binding are found when the basic ladder is mutated compared with the basic collar. n = 3, bars are ±SEM.

placed in cell culture and allowed to adhere to $Vcl^{-/-}$ MEFs. We subsequently pulled on the bead and tracked its movement. Cells expressing Vcl BL_2A or Vcl BL_4A exhibited an expected decrease in bead displacement, although the decrease was not statistically significant for Vcl BL_2A (Figure S5). These data suggest that Vcl lipid binding does not significantly regulate the cellular response at FAs to external force.

DISCUSSION

The lack of a strong experimentally validated structural model for the Vcl/PIP_2 interaction and contradictory biochemical and cellular data has hindered our understanding how PIP_2-dependent membrane association of Vcl contributes to Vcl functions (Chandrasekar et al., 2005; Diez et al., 2009; Halstead et al., 2010; Humphries et al., 2007; Saunders et al., 2006). The use of non-specific Vcl mutants has resulted in seemingly contradictory data (Chinthalapudi et al., 2014; Diez et al., 2009). While the crystal structure from Chinthalapudi et al. (2014, 2015) provides a starting model, the studies were conducted on a Vt mutant and a soluble short-chain PIP_2, which limits the extrapolation of the model to the interaction at a biological membrane.

Here, we provide an alternative model for how Vcl binds PIP_2 at a membrane. Our model is in agreement with published biochemical data: mutation at K944 and R945 or K1061 weakens PIP_2 binding by Vt (Chinthalapudi et al., 2014). However, according to our model, the basic collar and the basic ladder play unique roles in binding to PIP_2-containing membranes. While the basic ladder drives insertion into acidic membranes, the basic collar specifically recognizes PIP_2. The relative abilities of mutations at these sites to disrupt PIP_2- or PS-dependent liposome association are consistent with this model.

Our data further highlight the importance of the C terminus and the basic collar in F-actin crosslinking (Shen et al., 2011; Tolbert et al., 2014). The weaker actin filament crosslinking activity of Vt BC_2A and the nearly absent actin-crosslinking activity of Vt BC_4A and Vt BC_4Q suggest that residues R910, K915, K924, and R925 and their positive charge are integral to formation of the Vt dimer that facilitates actin bundling. As we did not see a decrease in the ability of MEFs to respond to external forces when expressing basic ladder Vcl variants, our data suggest that previous links to the Vcl/lipid interaction and mechanotransduction are due mainly to disruption of the ability of Vcl to crosslink actin (Diez et al., 2009). Indeed, it may be that the role of Vcl in mechanotransduction and cell stiffness is driven primarily by actin binding and crosslinking.

In addition, our NMR data suggest that PIP_2-C8 is a poor substitute for membrane-associated full-length PIP_2. Consistent with these observations, previous studies have shown that short-chain PIP_2 analogs bind to the PKCα C2 domain in a distinct manner from membrane-bound PIP_2 molecules (Guerrero-Valero et al., 2009; Lai et al., 2010). We find that PIP_2-C8 does not associate with the basic collar, but instead binds the basic ladder and the hydrophobic patch on helices 4 and 5, consistent with previous findings that the hydrophobic PIP_2-C8 acyl tails, rather than the head group, can drive binding (Pu et al., 2010). The nature of the lipid bilayer plays a significant role in the interaction of Vt with PIP_2 and future studies should account for this.

Our data support the use of basic ladder mutations to study the Vcl/PIP_2 interaction in cells (Cohen et al., 2005) given the actin-crosslinking defect exhibited by Vt constructs with mutations at the basic collar and the key role of the basic ladder in membrane insertion. However, care should be taken in interpretation of these results; mutation of the basic ladder appears sufficient to disrupt sustained interactions with a lipid bilayer, but may not prevent transient interactions with PIP_2. This, in addition to potential redundancies in FAs, may explain the lack of a strong cellular phenotype when disrupting the Vcl/PIP_2 interaction.

Our findings do provide evidence that PIP_2 binding contributes to Vcl activation (Golji et al., 2012; Ziegler et al., 2002), as lipid binding increases the fraction of activated Vcl at FAs. In addition, PIP_2 association increases the immobile fraction of Vcl, contrary to previous reports that PIP_2 binding recycles activated Vcl from FAs (Chinthalapudi et al., 2014). As PIP_2 binding enhances Vt

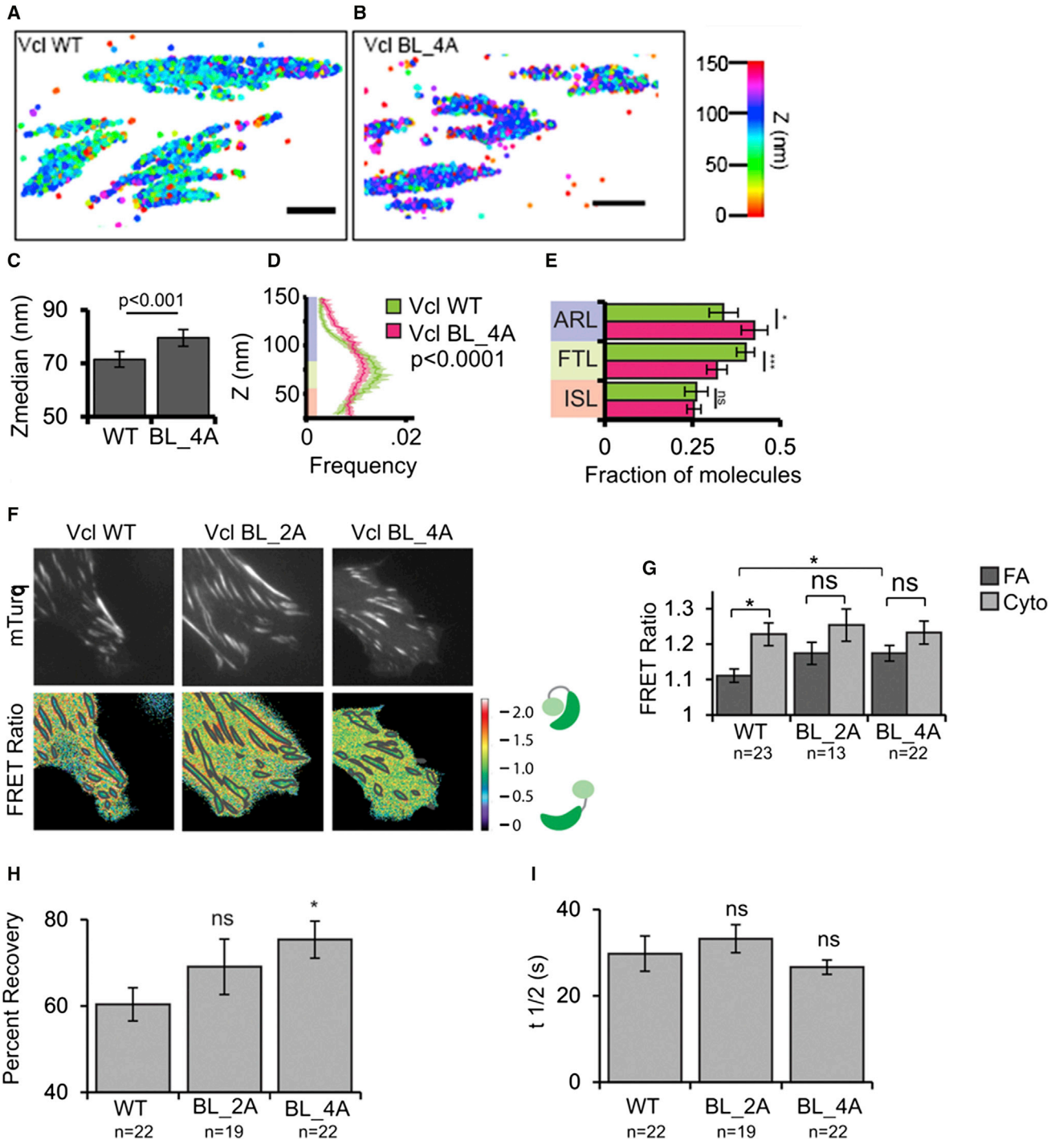

Figure 8. PIP_2 binding Regulates Vcl Nanoscale Localization, Activation, and Turnover in FAs

(A and B) Representative iPALM renderings for MEFs expressing Vcl WT-tdEos (A) or Vcl BL_4A-tdEos (B) are shown. The color scale represents Z position (nm), with FAs oriented with the distal tip facing right. Scale bar, 1 μm.

(C) Mean of Z median measurements from individual FAs.

(D) Averaged Z position frequency histograms of molecules within FAs. Solid line, mean frequency; shaded region, bootstrapped 95% confidence about the mean.

(E) Mean fraction of molecules localized to each of the three FA layers in FAs. Coloring in (D) and (E) is used to highlight the three FA layers. ISL, integrin signaling layer (red, 25–54 nm above the coverslip); FTL, force transduction layer (green, 55–84 nm above the coverslip); ARL, actin regulatory layer (purple, 85–150 nm above the coverslip). Graphs in (C), (D), and (E) represent measurements of n = 59 FAs from three Vcl WT-tdEos expressing cells and n = 58 FAs from six Vcl BL_4A-tdEos expressing cells.

(legend continued on next page)

phosphorylation by Src and PKCα (Ziegler et al., 2002), reduced association of Vcl with the membrane would also reduce the ability of these kinases to phosphorylate the tail domain, potentially increasing the fraction of Vcl that can revert to its autoinhibited conformation. This may explain the decreased activation and broader distribution of Vcl across FA layers. We previously showed that a constitutively active mutant of Vcl (D974/K975/R976/R978A) induced a strong shift in Vcl nanoscale localization from the integrin signaling layer to the actin regulatory (Case et al., 2015); our PIP_2 binding mutant induced a weaker shift from the integrin signaling layer to the force transduction layer. These findings suggest that Vcl/PIP_2 binding alone is not sufficient for full activation of Vcl in FAs. Rather, it is possible that PIP_2 binding "primes" Vcl for actin binding in the actin regulatory layer, but is dispensable for talin binding in the force transduction layer. There may be multiple conformations of Vcl that do not simply correspond to "active" or "inactive," which would correspond to the combinatorial interactions and post-translational modifications that regulate the conformation of Vcl at FAs. Our results further highlight the complex relationships between Vcl PIP_2 and FAs, and demonstrate a role of PIP_2 binding in Vcl activation, turnover, and localization of Vcl within FAs.

EXPERIMENTAL PROCEDURES

Expression and Purification of Vt

Vt expression constructs were a gift from Robert Liddington (Sanford Burnham Prebys Medical Discovery Institute). The pET15b Vt expression vector encodes a His-tag followed by a thrombin cleavage site and then chicken Vt residues 884–1,066. Vt was expressed and purified as described previously (Palmer et al., 2009; Thompson et al., 2014).

Lipid Co-sedimentation Assays

Vt binding to PIP_2 was evaluated by lipid co-sedimentation assays using small, unilamellar vesicles as reported previously (Palmer et al., 2009; Thompson et al., 2014). Details are provided in Supplemental Information.

Actin Co-sedimentation Assays

Actin co-sedimentation assays to assess actin-binding and actin-crosslinking (bundling) properties of Vt WT and Vt mutants were performed as reported previously (Shen et al., 2011).

Mutagenesis

Vt variants were generated using QuikChange Site-Directed Mutagenesis Kit (Stratagene) and the sequences were verified by DNA sequencing (GENEWIZ).

Computational Modeling

Modeling of the interaction of the PIP_2 head group with Vt (residues 896–1,055) was performed with MedusaDock (Ding et al., 2010; Yin et al., 2008). MedusaDock docking simulations constrain the Vt secondary structure but allow sampling of the Vt sidechain and PIP_2 head group using rotamer libraries, with the lowest energy pose reported.

Modeling of the interaction of the full PIP_2 molecule, 1-stearoyl-2-arachidonoyl-*sn*-glycero-3-phospho-(1′-myo-inositol-4′,5′-bisphosphate), with Vt in the absence of a lipid bilayer was performed with DMD simulations (Ding et al., 2008; Dokholyan et al., 1998; Shirvanyants et al., 2012). The initial docking pose was taken from the MedusaDock simulations. In these all-atom DMD simulations, Gō constraints were used to maintain intramolecular Cā/Cį contacts between Vt residues during the simulation. These constraints were applied for all residues in Vt or only residues in α helices in different simulations. The Gō constraints limit the potential for Vt unfolding while the PIP_2 is allowed to sample the protein surface. This combination allows for greater sampling of potential Vt:PIP_2 interactions while maintaining the structural integrity of Vt.

Modeling of the interaction of PIP_2 within a lipid bilayer was performed using all-atom, explicit solvent molecular dynamics simulations. A lipid bilayer of POPC with a single PIP_2 molecule was generated, and an initial pose of Vt (residues 896–1,055) bound to PIP_2 using the model generated from MedusaDock. Three simulations of Vt bound to PIP_2 in a POPC bilayer and three simulations of same configuration without PIP_2, each lasting 100 ns. were performed with GROMACS versus5.0.2 (Hess et al., 2008) using a CHARMM27 force field (Feller and MacKerell, 2000) with the following parameters: time-step of 2 fs, temperature of 300 K maintained by v-rescale thermostat with a time constant of 0.1 ps, 1 bar pressure maintained by semi-isotropic pressure coupling with 5 ps time constant, and particle mesh Ewald electrostatics.

NMR

NMR samples were prepared in 40 mM 2-(N-morpholino)ethanesulfonic acid (pH 5.5), 50 mM NaCl, 0.01% NaN_3, 2 mM DTT, and 5% D_2O. Samples contained 50 μM ^{15}N-enriched Vt with variable amounts of short-chain PIP_2 (1,2-dioctanoyl-*sn*-glycero-3-phospho-(1′-myo-inositol-4′,5′-bisphosphate; PIP_2-C8), Avanti Polar Lipids). NMR titrations and TRACT (Lee et al., 2006) experiments were collected on a 700 MHz Varian Inova magnet with a Bruker CryoProbe and console. ^{1}H-^{15}N 2D HSQC NMR experiments were performed to monitor the change in the backbone H-N signals (backbone assignments, BMRB: 15653) as a function of the short-chain PIP_2 ligand concentration (Palmer and Campbell, 2008). Further details can be found in Supplemental Information.

Cell Culture and Transfection

Vinculin knockout murine embryonic fibroblasts (Vcl$^{-/-}$ MEFs) were provided by Dr. Eileen Adamson (Burnham Institute, La Jolla, CA) and cultured, maintained, and transfected as reported previously (Tolbert et al., 2014).

FRAP Assays

FRAP experiments were performed with Vcl$^{-/-}$ MEFs expressing GFPEGF PEGFP-labeled Vcl WT or Vcl variants. Time-lapse total internal reflection fluorescence (TIRF) microscopy was performed at 37°C using an Apo TIRF 100× 1.49 numerical aperture oil immersion objective lens (Nikon Instruments) on an inverted Eclipse Ti microscope system (Nikon Instruments). EGFP images were captured with a CCD (CoolSNAP HQ2; Photometrics) operated in the 5 MHz readout mode using 488 nm laser illumination (Coherent). Cells were imaged for three frames at 5 s intervals prior to photobleaching, and then the 405 laser illumination of the FRAPPA system (Andor Technology) was used to bleach an entire FA in the protruding region of the cell. After photobleaching, cells were imaged at 2 s intervals for 1 min, and then at 5 s intervals for 3 min. Final images were drift corrected using the rigid body method of the StackReg ImageJ plugin (Thevenaz et al., 1998), and the mean intensity inside individual bleached FAs was corrected for imaging-induced photobleaching using a cytoplasmic region outside of the bleached region. Fluorescence recovery was fit with a single exponential to determine the $T_{1/2}$ and

(F) Localization and FRET signal of Vcl constructs. mTurquoise (mTurq, top) and processed mTurquoise/NeonGreen FRET ratio image (bottom) of Vcl$^{-/-}$ MEFs expressing either WT, BL_2A, or BL_4A Vcl FRET biosensors. The FA mask (gray lines) was created from the mTurq image and superimposed onto the FRET ratio image.

(G) Quantification of the mean FRET ratio value inside FAs (FA) and outside FAs (Cyto).

(H and I) FRAP measurements of Vcl constructs. Mean percent recovery (H) and $T_{1/2}$ (I) of Vcl obtained from single exponential fits of FRAP recovery curves. The fraction of Vcl that turns over at FAs (mobile fraction) increases upon disruption of lipid binding. Data in all bar graphs are represented as mean ±95% confidence intervals. In (G), (H), and (I), n = number of cells measured and significance is tested with ANOVA test followed by Tukey's test post hoc analysis. Difference is significant at *$p < 0.05$ cutoff; ***$p < 0.001$; ns, not significant. See also Figures S4–S6.

percent recovery of each FA. Cells that retracted after bleaching were discarded from the analysis.

FRET Assays

FRET experiments were performed using wide-field epifluorescence as described previously (Chen et al., 2005). In brief, a Vcl activation FRET biosensor in which fluorophores were inserted into the Vcl protein between the head and tail (mTurquoise, donor) and that the C terminus (mNeonGreen37, acceptor) such that FRET occurs when Vt interacts with the Vcl head in the autoinhibited conformation and FRET decreases when autoinhibition is relieved and Vcl is activated (Case et al., 2015). The raw mTurquoise, FRET and Neon Green images were aligned using the rigid body method of the StackReg ImageJ plugin (Thevenaz et al., 1998). The FRET ratio was calculated using MATLAB to run the Danuser Lab Biosensors Processing Software 2.1 (available for download: http://lccb.hms.harvard.edu/software.html). Differences between mean FRET ratios were determined by an ANOVA followed by Tukey's post hoc analysis and differences were considered significant at $p < 0.05$.

iPALM

Interference photoactivation localization microscopy (iPALM) imaging of $Vcl^{-/-}$ MEF expressing Vcl WT or Vcl variants containing an N-terminal tdEos fluorophore was performed as described previously (Case et al., 2015). After image acquisition was complete, the raw datasets were processed to localize individual molecules and extract their x, y, and z coordinates, and analyzed in MATLAB as described previously (Case et al., 2015). Representative iPALM images were rendered with the PALMsiever MATLAB package (Pengo et al., 2015) using the 3D Hue rendering technique to represent the Z position with color. Additional Experimental Procedures can be found in Supplemental Information.

SUPPLEMENTAL INFORMATION

Supplemental Information includes Supplemental Experimental Procedures, six figures, and three movies and can be found with this article online at http://dx.doi.org/10.1016/j.str.2016.12.002.

AUTHOR CONTRIBUTIONS

S.L.C., N.V.D., and C.M.W. conceived and supervised the research. Computational modeling and simulations were performed by S.R. and A.T. Biochemical experiments were performed by P.M.T. and M.P. Cellular experiments were performed by C.E.T. and L.B.C. Data were analyzed by P.M.T., C.E.T., L.B.C., S.R., A.T., and M.P. P.M.T., C.E.T, and L.B.C. wrote the manuscript with discussion and improvements from all authors.

ACKNOWLEDGMENTS

P.M.T. was supported by the American Heart Association (12PRE11820012). Funding to S.L.C. and N.V.D. was supported by the NIH (1R01GM115597). Funding to C.E.T. was supported by the NIH (GM029860). The authors wish to thank Evan Nelsen, Greg Young, and Paul Sapienza for their assistance with methods as well as Keith Burridge for his feedback on the manuscript.

Received: June 21, 2016
Revised: November 10, 2016
Accepted: December 12, 2016
Published: January 12, 2017

REFERENCES

Bakolitsa, C., de Pereda, J.M., Bagshaw, C.R., Critchley, D.R., and Liddington, R.C. (1999). Crystal structure of the vinculin tail suggests a pathway for activation. Cell *99*, 603–613.

Bakolitsa, C., Cohen, D.M., Bankston, L.A., Bobkov, A.A., Cadwell, G.W., Jennings, L., Critchley, D.R., Craig, S.W., and Liddington, R.C. (2004). Structural basis for vinculin activation at sites of cell adhesion. Nature *430*, 583–586.

Case, L.B., and Waterman, C.M. (2015). Integration of actin dynamics and cell adhesion by a three-dimensional, mechanosensitive molecular clutch. Nat. Cell Biol. *17*, 955–963.

Case, L.B., Baird, M.A., Shtengel, G., Campbell, S.L., Hess, H.F., Davidson, M.W., and Waterman, C.M. (2015). Molecular mechanism of vinculin activation and nanoscale spatial organization in focal adhesions. Nat. Cell Biol. *17*, 880–892.

Chandrasekar, I., Stradal, T.E., Holt, M.R., Entschladen, F., Jockusch, B.M., and Ziegler, W.H. (2005). Vinculin acts as a sensor in lipid regulation of adhesion-site turnover. J. Cell Sci. *118*, 1461–1472.

Chen, H., Cohen, D.M., Choudhury, D.M., Kioka, N., and Craig, S.W. (2005). Spatial distribution and functional significance of activated vinculin in living cells. J. Cell Biol. *169*, 459–470.

Chen, H., Choudhury, D.M., and Craig, S.W. (2006). Coincidence of actin filaments and talin is required to activate vinculin. J. Biol. Chem. *281*, 40389–40398.

Chinthalapudi, K., Rangarajan, E.S., Patil, D.N., George, E.M., Brown, D.T., and Izard, T. (2014). Lipid binding promotes oligomerization and focal adhesion activity of vinculin. J. Cell Biol. *207*, 643–656.

Chinthalapudi, K., Patil, D.N., Rangarajan, E.S., Rader, C., and Izard, T. (2015). Lipid-directed vinculin dimerization. Biochemistry *54*, 2758–2768.

Cohen, D.M., Chen, H., Johnson, R.P., Choudhury, B., and Craig, S.W. (2005). Two distinct head-tail interfaces cooperate to suppress activation of vinculin by talin. J. Biol. Chem. *280*, 17109–17117.

Cohen, D.M., Kutscher, B., Chen, H., Murphy, D.B., and Craig, S.W. (2006). A conformational switch in vinculin drives formation and dynamics of a talin-vinculin complex at focal adhesions. J. Biol. Chem. *281*, 16006–16015.

Coll, J.L., Ben-Ze'ev, A., Ezzell, R.M., Rodriguez Fernandez, J.L., Baribault, H., Oshima, R.G., and Adamson, E.D. (1995). Targeted disruption of vinculin genes in F9 and embryonic stem cells changes cell morphology, adhesion, and locomotion. Proc. Natl. Acad. Sci. USA *92*, 9161–9165.

Diez, G., Kollmannsberger, P., Mierke, C.T., Koch, T.M., Vali, H., Fabry, B., and Goldmann, W.H. (2009). Anchorage of vinculin to lipid membranes influences cell mechanical properties. Biophys. J. *97*, 3105–3112.

Ding, F., Tsao, D., Nie, H., and Dokholyan, N.V. (2008). Ab initio folding of proteins with all-atom discrete molecular dynamics. Structure *16*, 1010–1018.

Ding, F., Yin, S., and Dokholyan, N.V. (2010). Rapid flexible docking using a stochastic rotamer library of ligands. J. Chem. Inf. Model. *50*, 1623–1632.

Dokholyan, N.V., Buldyrev, S.V., Stanley, H.E., and Shakhnovich, E.I. (1998). Discrete molecular dynamics studies of the folding of a protein-like model. Fold Des. *3*, 577–587.

Feller, S.E., and MacKerell, A.D. (2000). An improved empirical potential energy function for molecular simulations of phospholipids. J. Phys. Chem. B *104*, 7510–7515.

Golji, J., Wendorff, T., and Mofrad, M.R.K. (2012). Phosphorylation primes vinculin for activation. Biophys. J. *102*, 2022–2030.

Guerrero-Valero, M., Ferrer-Orta, C., Querol-Audi, J., Marin-Vicente, C., Fita, I., Gomez-Fernandez, J.C., Verdaguer, N., and Corbalan-Garcia, S. (2009). Structural and mechanistic insights into the association of PKCalpha-C2 domain to PtdIns(4,5)P2. Proc. Natl. Acad. Sci. USA *106*, 6603–6607.

Halstead, J.R., Savaskan, N.E., van den Bout, I., Van Horck, F., Hajdo-Milasinovic, A., Snell, M., Keune, W.J., Ten Klooster, J.P., Hordijk, P.L., and Divecha, N. (2010). Rac controls PIP5K localisation and PtdIns(4,5)P(2) synthesis, which modulates vinculin localisation and neurite dynamics. J. Cell Sci. *123*, 3535–3546.

Hess, B., Kutzner, C., van der Spoel, D., and Lindahl, E. (2008). GROMACS 4: algorithms for highly efficient, load-balanced, and scalable molecular simulation. J. Chem. Theor. Comput. *4*, 435–447.

Humphries, J.D., Wang, P., Streuli, C., Geiger, B., Humphries, M.J., and Ballestrem, C. (2007). Vinculin controls focal adhesion formation by direct interactions with talin and actin. J. Cell Biol. *179*, 1043–1057.

Huttelmaier, S., Bubeck, P., Rudiger, M., and Jockusch, B.M. (1997). Characterization of two F-actin-binding and oligomerization sites in the cell-contact protein vinculin. Eur. J. Biochem. *247*, 1136–1142.

Izard, T., Evans, G., Borgon, R.A., Rush, C.L., Bricogne, G., and Bois, P.R. (2004). Vinculin activation by talin through helical bundle conversion. Nature *427*, 171–175.

Johnson, R.P., and Craig, S.W. (1995a). The carboxy-terminal tail domain of vinculin contains a cryptic binding site for acidic phospholipids. Biochem. Biophys. Res. Commun. *210*, 159–164.

Johnson, R.P., and Craig, S.W. (1995b). F-actin binding site masked by the intramolecular association of vinculin head and tail domains. Nature *373*, 261–264.

Johnson, R.P., Niggli, V., Durrer, P., and Craig, S.W. (1998). A conserved motif in the tail domain of vinculin mediates association with and insertion into acidic phospholipid bilayers. Biochemistry *37*, 10211–10222.

Kanchanawong, P., Shtengel, G., Pasapera, A.M., Ramko, E.B., Davidson, M.W., Hess, H.F., and Waterman, C.M. (2010). Nanoscale architecture of integrin-based cell adhesions. Nature *468*, 580–584.

Kim, L.Y., Thompson, P.M., Campbell, S.L., and Alushin, G.M. (2014). Structural Basis of the Vinculin–F-Actin Interaction (American Society for Cell Biology).

Lai, C.L., Landgraf, K.E., Voth, G.A., and Falke, J.J. (2010). Membrane docking geometry and target lipid stoichiometry of membrane-bound PKCalpha C2 domain: a combined molecular dynamics and experimental study. J. Mol. Biol. *402*, 301–310.

le Duc, Q., Shi, Q., Blonk, I., Sonnenberg, A., Wang, N., Leckband, D., and de Rooij, J. (2010). Vinculin potentiates E-cadherin mechanosensing and is recruited to actin-anchored sites within adherens junctions in a myosin II-dependent manner. J. Cell Biol. *189*, 1107–1115.

Lee, D., Hilty, C., Wider, G., and Wuthrich, K. (2006). Effective rotational correlation times of proteins from NMR relaxation interference. J. Magn. Reson. *178*, 72–76.

Legate, K.R., Takahashi, S., Bonakdar, N., Fabry, B., Boettiger, D., Zent, R., and Fassler, R. (2011). Integrin adhesion and force coupling are independently regulated by localized PtdIns(4,5)2 synthesis. EMBO J. *30*, 4539–4553.

Li, X., Zhou, Q., Sunkara, M., Kutys, M.L., Wu, Z., Rychahou, P., Morris, A.J., Zhu, H., Evers, B.M., and Huang, C. (2013). Ubiquitylation of phosphatidylinositol 4-phosphate 5-kinase type I gamma by HECTD1 regulates focal adhesion dynamics and cell migration. J. Cell Sci. *126*, 2617–2628.

Ling, K., Doughman, R.L., Firestone, A.J., Bunce, M.W., and Anderson, R.A. (2002). Type I gamma phosphatidylinositol phosphate kinase targets and regulates focal adhesions. Nature *420*, 89–93.

Liu, J., Wang, Y., Goh, W.I., Goh, H., Baird, M.A., Ruehland, S., Teo, S., Bate, N., Critchley, D.R., Davidson, M.W., et al. (2015). Talin determines the nanoscale architecture of focal adhesions. Proc. Natl. Acad. Sci. USA *112*, E4864–E4873.

Marquez, M.G., Fernandez-Tome Mdel, C., Favale, N.O., Pescio, L.G., and Sterin-Speziale, N.B. (2009). Bradykinin induces formation of vesicle-like structures containing vinculin and PtdIns(4,5)P2 in renal papillary collecting duct cells. Am. J. Physiol. Ren. Physiol. *297*, F1181–F1191.

Mierke, C.T., Kollmannsberger, P., Zitterbart, D.P., Smith, J., Fabry, B., and Goldmann, W.H. (2008). Mechano-coupling and regulation of contractility by the vinculin tail domain. Biophys. J. *94*, 661–670.

Palmer, S.M., and Campbell, S.L. (2008). Backbone 1H, 13C, and 15N NMR assignments of the tail domain of vinculin. Biomol. NMR Assign. *2*, 69–71.

Palmer, S.M., Playford, M.P., Craig, S.W., Schaller, M.D., and Campbell, S.L. (2009). Lipid binding to the tail domain of vinculin: specificity and the role of the N and C termini. J. Biol. Chem. *284*, 7223–7231.

Pengo, T., Holden, S.J., and Manley, S. (2015). PALMsiever: a tool to turn raw data into results for single-molecule localization microscopy. Bioinformatics *31*, 797–798.

Proctor, E.A., Ding, F., and Dokholyan, N.V. (2011). Structural and thermodynamic effects of post-translational modifications in mutant and wild type Cu, Zn superoxide dismutase. J. Mol. Biol. *408*, 555–567.

Pu, M., Orr, A., Redfield, A.G., and Roberts, M.F. (2010). Defining specific lipid binding sites for a peripheral membrane protein in situ using subtesla field-cycling NMR. J. Biol. Chem. *285*, 26916–26922.

Saunders, R.M., Holt, M.R., Jennings, L., Sutton, D.H., Barsukov, I.L., Bobkov, A., Liddington, R.C., Adamson, E.A., Dunn, G.A., and Critchley, D.R. (2006). Role of vinculin in regulating focal adhesion turnover. Eur. J. Cell Biol. *85*, 487–500.

Shen, K., Tolbert, C.E., Guilluy, C., Swaminathan, V.S., Berginski, M.E., Burridge, K., Superfine, R., and Campbell, S.L. (2011). The vinculin C-terminal hairpin mediates F-actin bundle formation, focal adhesion, and cell mechanical properties. J. Biol. Chem. *286*, 45103–45115.

Shirvanyants, D., Ding, F., Tsao, D., Ramachandran, S., and Dokholyan, N.V. (2012). Discrete molecular dynamics: an efficient and versatile simulation method for fine protein characterization. J. Phys. Chem. B *116*, 8375–8382.

Sun, Y., Ling, K., Wagoner, M.P., and Anderson, R.A. (2007). Type I gamma phosphatidylinositol phosphate kinase is required for EGF-stimulated directional cell migration. J. Cell Biol. *178*, 297–308.

Thevenaz, P., Ruttimann, U.E., and Unser, M. (1998). A pyramid approach to subpixel registration based on intensity. IEEE Trans. Image Process. *7*, 27–41.

Thompson, P.M., Tolbert, C.E., Shen, K., Kota, P., Palmer, S.M., Plevock, K.M., Orlova, A., Galkin, V.E., Burridge, K., Egelman, E.H., et al. (2014). Identification of an actin binding surface on vinculin that mediates mechanical cell and focal adhesion properties. Structure *22*, 697–706.

Tolbert, C.E., Thompson, P.M., Superfine, R., Burridge, K., and Campbell, S.L. (2014). Phosphorylation at Y1065 in vinculin mediates actin bundling, cell spreading, and mechanical responses to force. Biochemistry *53*, 5526–5536.

van den Bout, I., and Divecha, N. (2009). PIP5K-driven PtdIns(4,5)P2 synthesis: regulation and cellular functions. J. Cell Sci. *122*, 3837–3850.

Weekes, J., Barry, S.T., and Critchley, D.R. (1996). Acidic phospholipids inhibit the intramolecular association between the N- and C-terminal regions of vinculin, exposing actin-binding and protein kinase C phosphorylation sites. Biochem. J. *314*, 827–832.

Wirth, V.F., List, F., Diez, G., and Goldmann, W.H. (2010). Vinculin's C-terminal region facilitates phospholipid membrane insertion. Biochem. Biophys. Res. Commun. *398*, 433–437.

Wu, Z., Li, X., Sunkara, M., Spearman, H., Morris, A.J., and Huang, C. (2011). PIPKIgamma regulates focal adhesion dynamics and colon cancer cell invasion. PLoS One *6*, e24775.

Xu, W., Baribault, H., and Adamson, E.D. (1998a). Vinculin knockout results in heart and brain defects during embryonic development. Development *125*, 327–337.

Xu, W., Coll, J.L., and Adamson, E.D. (1998b). Rescue of the mutant phenotype by reexpression of full-length vinculin in null F9 cells; effects on cell locomotion by domain deleted vinculin. J. Cell Sci. *111*, 1535–1544.

Yin, S., Biedermannova, L., Vondrasek, J., and Dokholyan, N.V. (2008). MedusaScore: an accurate force field-based scoring function for virtual drug screening. J. Chem. Inf. Model. *48*, 1656–1662.

Ziegler, W.H., Tigges, U., Zieseniss, A., and Jockusch, B.M. (2002). A lipid-regulated docking site on vinculin for protein kinase C. J. Biol. Chem. *277*, 7396–7404.

Structure, Volume *25*

Supplemental Information

A Structural Model for Vinculin Insertion into PIP_2-Containing Membranes and the Effect of Insertion on Vinculin Activation and Localization

Peter M. Thompson, Srinivas Ramachandran, Lindsay B. Case, Caitlin E. Tolbert, Arpit Tandon, Mihir Pershad, Nikolay V. Dokholyan, Clare M. Waterman, and Sharon L. Campbell

Supplemental Figures

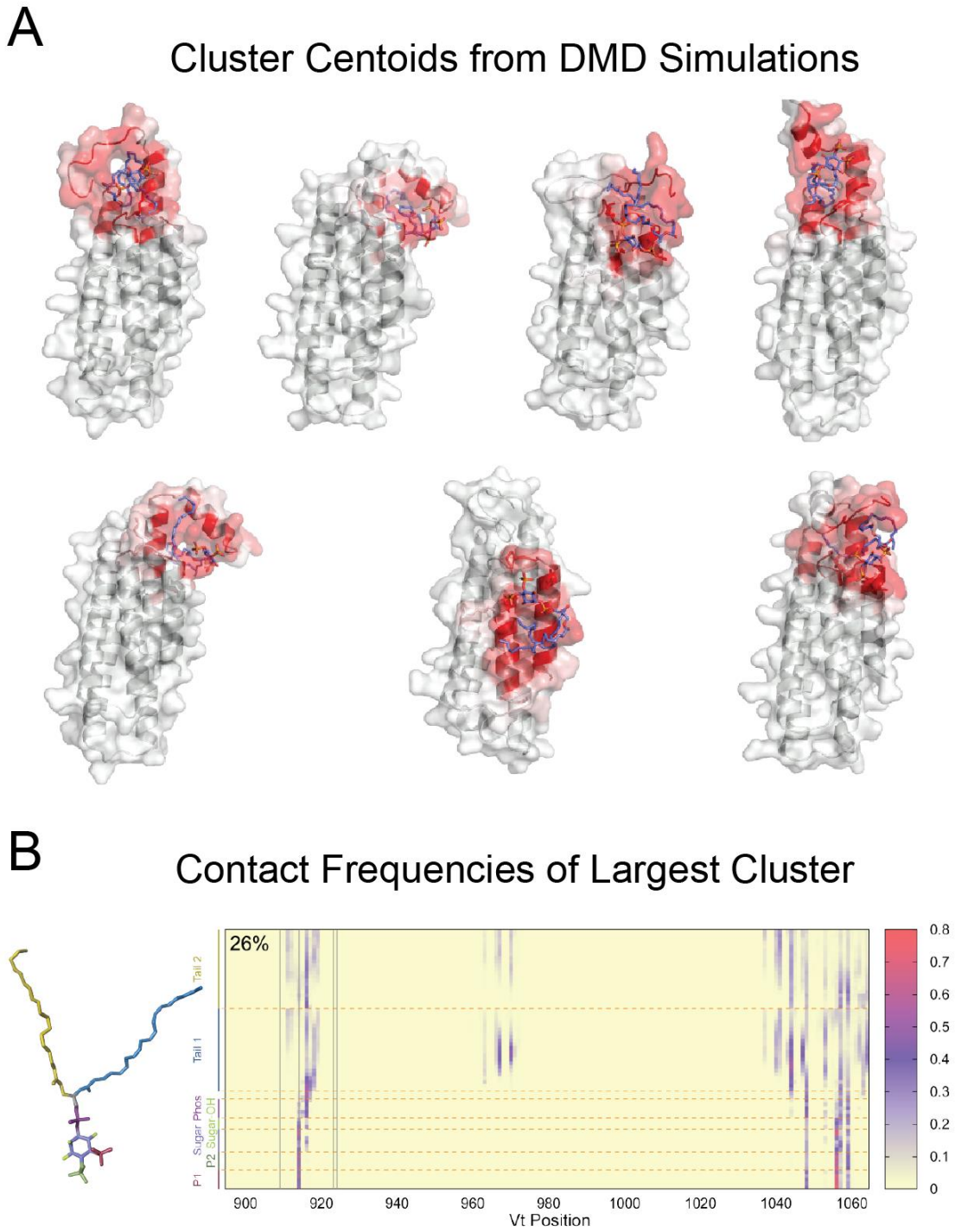

Figure S1, related to Figure 2. DMD simulations of Vt and unrestrained PIP_2.
A) Representative structures from seven clusters generated from the DMD simulation. Four of the seven clusters feature contacts between PIP_2 and basic collar. B) Heat map of contacts between Vt residues and atoms of PIP_2. Most contacts are observed between PIP_2 and the basic collar.

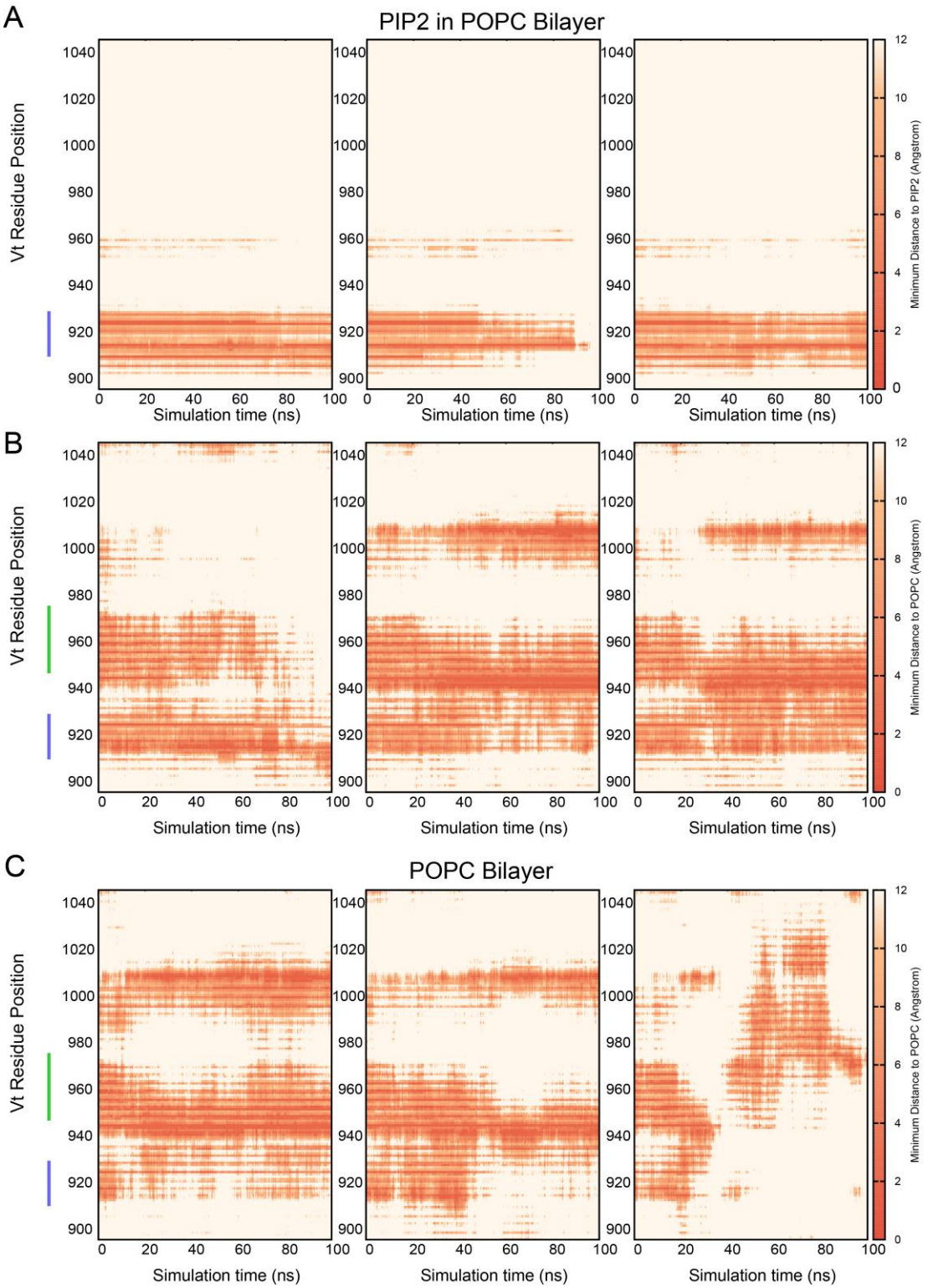

Figure S2, related to Figure 2. MD simulations of Vt in a POPC bilayer in the absence and presence of PIP_2. Heat maps displaying minimum distance between residues of Vt and (A) PIP_2 or (B) POPC, as a function of simulation time. Panel C is a heat map highlighting the minimum distance between residues of Vt and POPC in the absence of PIP_2 as a function of simulation time. The blue line marks residues of the basic collar that contact PIP_2. The green line denotes helix 3 residues. Three heat maps in each row represent three independent simulations of 100 ns each.

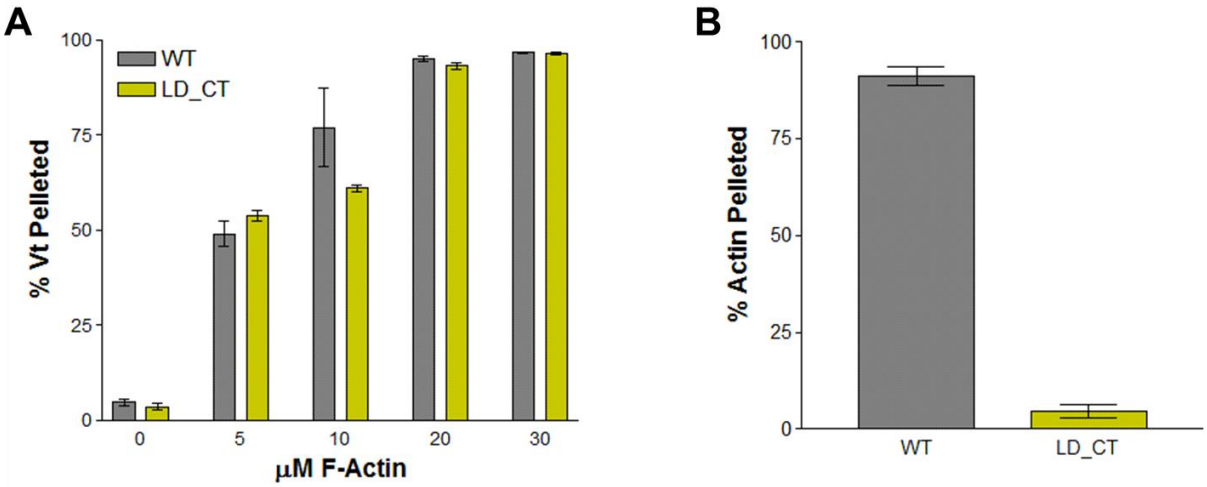

Figure S3, related to Figure 5. Actin-binding and crosslinking capacity of Vt LD-CT (R1060Q/K1061Q).

Results from actin co-sedimentation assays evaluating the ability of Vt LD-CT to bind (A) and crosslink (B) F-actin. Vt LD-CT retains F-actin binding, but is significantly impaired in its ability to crosslink F-actin. N=3, bars are ± SEM.

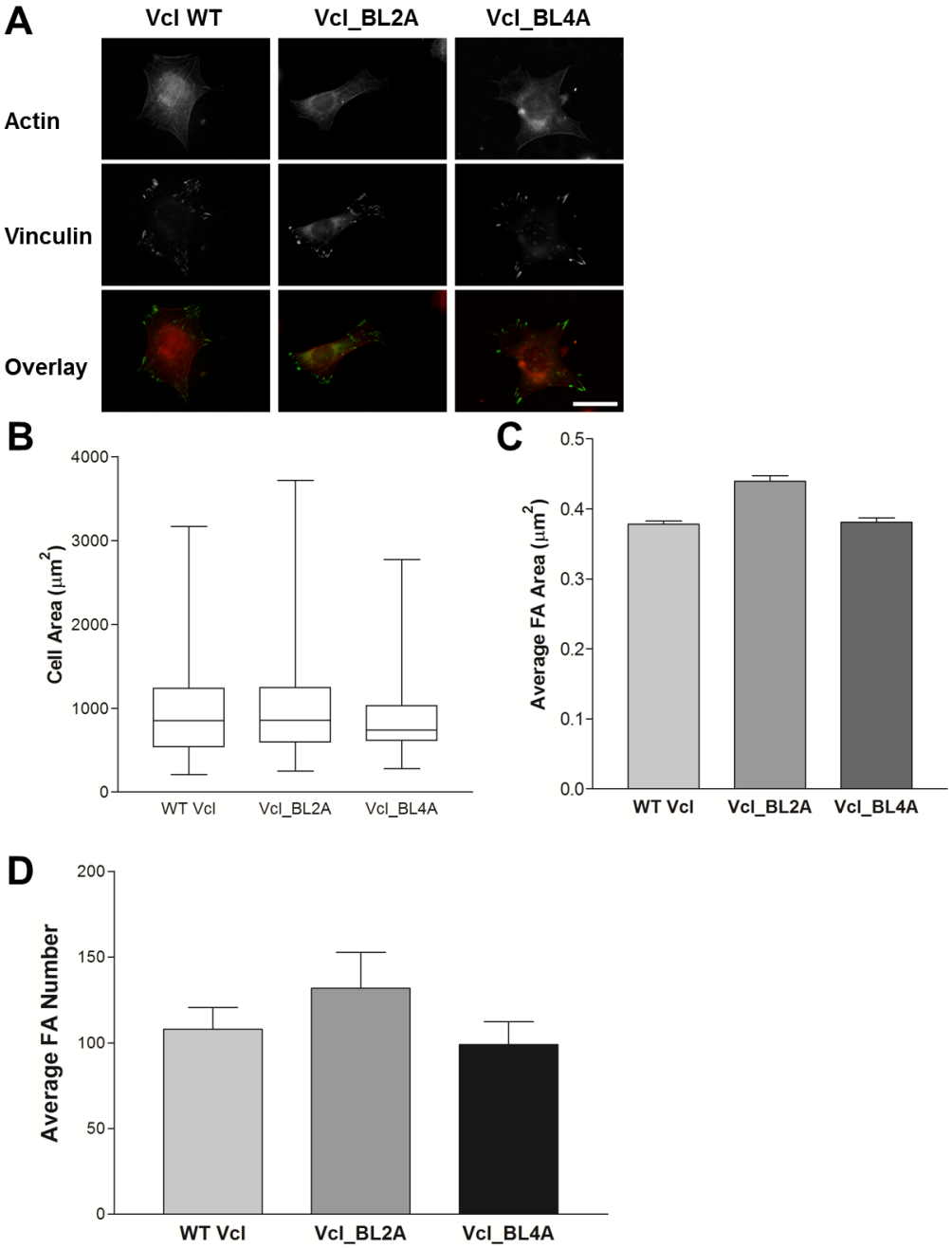

Figure S4, related to Figure 8. Lipid binding to Vcl does not alter FA size, FA number, or cellular size.

(A) Vcl -/- MEFs expressing Vcl WT, Vcl_BL2A, or Vcl_BL4A exhibit normal Vcl recruitment to FAs and do not show significant impairment in the actin cytoskeleton. Representative images are shown. Scale bar is 20 μm. (B) Vcl -/- MEFs expressing Vcl WT, Vcl_BL2A, or Vcl_BL4A are not significantly different in size. Data are represented as a box plot (n=74, 53, and 45, respectively, for Vcl WT, Vcl_BL2A, and Vcl_BL4A). (C,D) Vcl -/- MEFs expressing Vcl WT, Vcl_BL2A, or Vcl_BL4A do not exhibit significant differences in the average FA size (C) or the average number of FAs per cell (D). Data are shown as the average ± SEM (n = 53, 28, 26 cells for Vcl WT, Vcl_BL2A, and Vcl_BL4A, respectively).

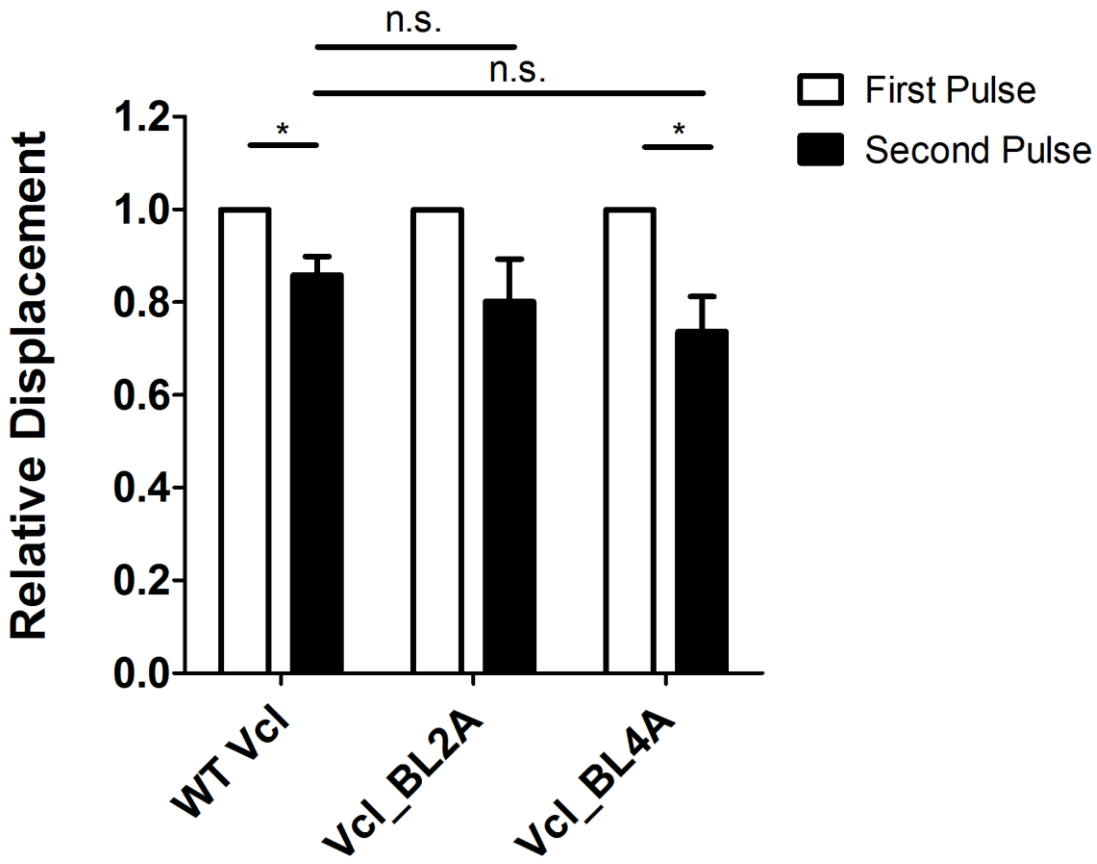

Figure S5, related to Figure 8. Lipid binding to Vcl does not alter cellular response to external forces.

3DFM experiments were used to test the reinforcement at FAs in Vcl -/- MEFs expressing Vcl constructs upon successive pulses of force. Vcl -/- MEFs expressing Vcl variants did not show significant impairment in their ability to reinforce FAs. Error bars are ± SEM (n=31, 8, 11 for Vcl WT, Vcl_BL2A, Vcl_BL4A, respectively; * for p-value < 0.01; n.s. for p > 0.05).

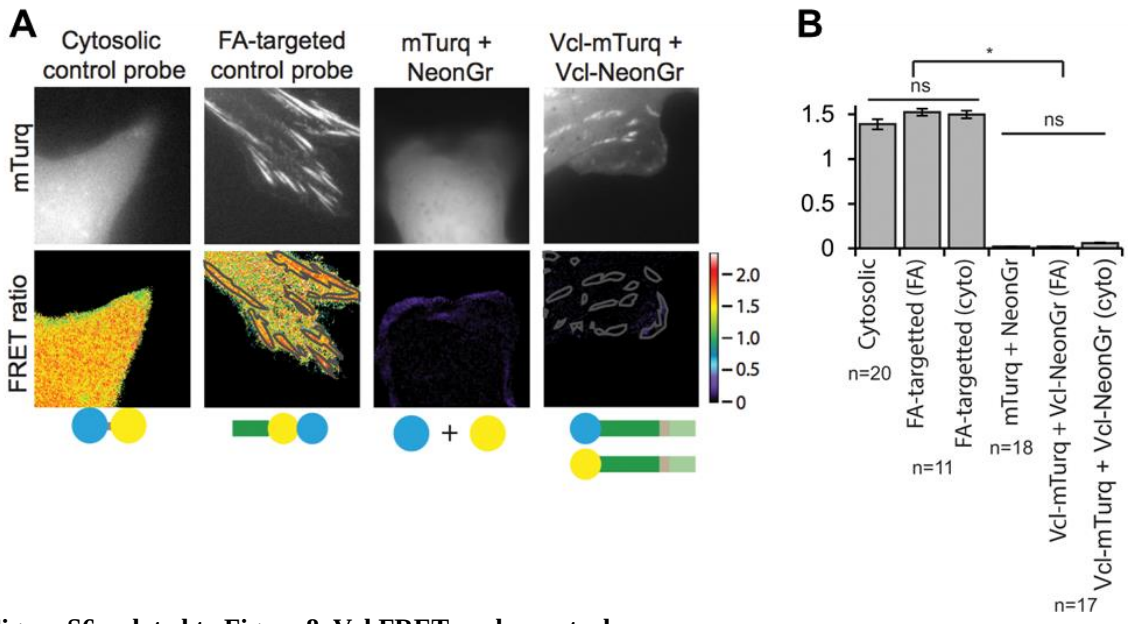

Figure S6, related to Figure 8. Vcl FRET probe controls.

Images of Vcl-/- MEFs expressing various FRET probes. (A) mTurquoise (mTurq, top) and processed mTurquouise/NeonGreen FRET ratio image (bottom) of Vcl-/- MEFs expressing various FRET probes. Cartoon schematics of the probes used are shown below the FRET images. The FA mask (grey lines) was created from the mTurq image and superimposed onto the FRET ratio image. (B) Quantification of the mean FRET ratio value in the entire cell, or inside FAs (FA) and outside FAs (Cyto). n = number of cells measured and significance is tested with ANOVA test followed by Tukey test post-hoc analysis. (* difference is significant at $p<0.05$ cutoff, ns: not significant). Error bars are ± 95% confidence intervals.

Supplemental Movies

Movie S1: Side view of 100 ns simulation of Vt interacting with a PIP_2-containing POPC bilayer, related to Figure 2.

Side view (one of three 100 ns simulations) of Vt interacting with a POPC bilayer containing PIP_2. POPC is shown in sticks with gray carbons. PIP_2 is shown as spheres with blue carbons. Vinculin is shown as a green ribbon. The time between frames is 2.5 ns.

Movie S2: Top view of 100 ns simulation of Vt interacting with a PIP_2-containing POPC bilayer, related to Figure 2.

A top-down view of the same simulation shown in Movie S1..

Movie S3: Side view of 100 ns simulation of Vt interacting with a POPC bilayer, related to Figure 2.

Side view (one the three 100 ns simulations) of Vt interacting with a POPC bilayer without PIP_2. POPC is shown in sticks with gray carbons. Vinculin is shown as a green ribbon. The time between frames is 2.5 ns.

Supplemental Experimental Procedures

Lipid co-sedimentation assays

SUVs were composed of 250 µg lipid mixture, with the reported PIP_2% using a 3:1:1 ratio of phosphatidylethanolamine:phosphatidylcholine:PS and/or PIP_2. The lipids (Avanti Polar Lipids, Alabaster, AL, USA) were resuspended by vortexing in lipid co-sedimentation buffer (40 mM MES pH 6.0, 150 mM NaCl, and 2 mM dithiotheitol (DTT)) and subsequently extruded in a mini-extruder (Avanti Polar Lipids) to produce the SUVs. Relative protein amounts were quantified using ImageJ (Abramoff et al., 2004).

Binding to PS was evaluated similarly. When assembling SUVs, the reported percentage of PS was used, and the remaining fraction of lipids contain a 3:1 mixture of phoshphatidylethanolamine:phosphatidylcholine.

Cell imaging and FA analysis

Cell imaging and FA analyses were performed as previously described (Tolbert et al., 2014). Briefly, prior to seeding, cells were serum-starved in Dulbecco's Modified Eagle Medium supplemented with 0.5% delipidated bovine serum albumin (Sigma) and antiobiotic-antimycotic solution. Cells were then resuspended in the serum-free media for approximately 2 hours before seeding onto glass coverslips coated with 50 µg/mL fibronectin (FN) for 2 hours. Cells were then fixed for 10 minutes with 3.7% formaldehyde and washed with 1X phosphate-buffered saline (PBS) followed by permeabilization for 10 minutes with 0.2% Triton X-100 in PBS and stained with phalloidin (Invitrogen, Carlsbad, CA). Coverslips were examined with a Zeiss Axiovert 200M microscope with a 63X objective lens and a Hamamatsu ORCA-ERAG digital camera. Cell area and FAs were quantified as previously reported (Shen et al., 2011). Experiments were repeated three independent times with the data represented as the mean ± SEM. Data sets were analyzed by the two-tailed Student's t test for p-values.

Force Microscopy.

Three-dimensional force microscopy (3DFM) was used to apply controlled force through magnetic beads coated with FN to engaged integrins in order to track bead displacements as a readout of cellular reinforcement. Experiments and analysis were performed as previously described (Izard et al., 2004). Bead displacements were analyzed using the two-tailed Student's t test for p-values and are reported as mean ± SEM.

Further NMR details

Chemical shift changes were tracked and chemical shift perturbations (CSP) were calculated as described (Thompson et al., 2015). To compensate for the larger chemical shift range in the ^{15}N dimension, ^{15}N chemical shifts were scaled by a factor of 9.87.

[^{15}N, ^{1}H]TRACT experiments (Lee et al., 2006) were collected using delay times of from 2 to 98 ms at 4 ms intervals. 1D spectra were integrated using Bruker Topspin software. The data were analyzed by

fitting to an exponential decay curve with a non-zero plateau. The relaxation rates were then used to calculate the effective rotational correlation times and 100 Monte Carlo simulations were used to estimate error in the calculations.

Further details of iPALM

Briefly, to use the position of the coverslip as a reference point, the measured Z-position of the coverslip was set to 0 for each imaged cell. To compare different conditions, the average Z-median, average Z-distribution and average percent of molecules in each FA layer was calculated, and 95% confidence intervals were computed by resampling the datasets 10,000 times using the Bootstrapping method. Confidence intervals are displayed as error bars on bar graphs or as lightly shaded regions on the average Z-distribution plots.

Supplemental References

Abramoff, M.D., Magalhaes, P.J., and Ram, S.J. (2004). Image Processing with ImageJ. Biophotonics International *11*, 36-42.

Izard, T., Evans, G., Borgon, R.A., Rush, C.L., Bricogne, G., and Bois, P.R. (2004). Vinculin activation by talin through helical bundle conversion. Nature *427*, 171-175.

Lee, D., Hilty, C., Wider, G., and Wuthrich, K. (2006). Effective rotational correlation times of proteins from NMR relaxation interference. J Magn Reson *178*, 72-76.

Shen, K., Tolbert, C.E., Guilluy, C., Swaminathan, V.S., Berginski, M.E., Burridge, K., Superfine, R., and Campbell, S.L. (2011). The vinculin C-terminal hairpin mediates F-actin bundle formation, focal adhesion, and cell mechanical properties. J Biol Chem *286*, 45103-45115.

Thompson, P.M., Beck, M.R., and Campbell, S.L. (2015). Protein-protein interaction analysis by nuclear magnetic resonance spectroscopy. Methods Mol Biol *1278*, 267-279.

Tolbert, C.E., Thompson, P.M., Superfine, R., Burridge, K., and Campbell, S.L. (2014). Phosphorylation at Y1065 in Vinculin Mediates Actin Bundling, Cell Spreading, and Mechanical Responses to Force. Biochemistry.